ISSN 2709-3409 (Online)

JOURNAL OF TERTIARY AND INDUSTRIAL SCIENCES

TERTIARY SCIENCES

GEOLOGY AND MINES

A MULTIDISCIPLINARY JOURNAL OF THE HIGHER TECHNICAL TEACHERS' TRAINING COLLEGE, KUMBA

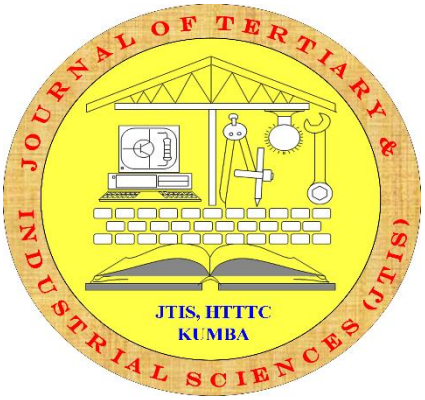

VOLUME 6, NUMBER 3
AUGUST, 2026

PUBLISHER:
HIGHER TECHNICAL TEACHERS' TRAINING COLLEGE (HTTTC)
UNIVERSITY OF BUEA
P.O Box: 249 Buea Road, Kumba
Tel: (+237) 33354691 – Fax: (+237) 33354692
Email: editor@jtis-htttcubuea.com
Website: https://www.jtis-htttcubuea.com

Journal of Tertiary and Industrial Sciences *Vol. 6, No. 3, 2026*
ISSN 2709-3409 (Online)

EDITORIAL BOARD

Journal of Tertiary and Industrial Sciences *Vol. 6, No. 3, 2026*
ISSN 2709-3409 (Online)

Journal of Tertiary and Industrial Sciences *Vol. 6, No. 3, 2026*
ISSN 2709-3409 (Online)

CONTENTS

Journal of Tertiary and Industrial Sciences *Vol. 6, No. 3, 2026*
ISSN 2709-3409 (Online)

Petrogenetic characterization of banded iron formations of the Nyong Complex, Southern Cameroon: implications for the origin and depositional setting of Paleoproterozoic Iron Formations

Ndema Mbongué Jean-Lavenir[1], Djomo Michel Cedric[1], Sigué Cyrille[1], Nga Essomba Tsoungui, Philomène Estelle[2], Christian Diomo Mukete[1], Peter Namange[1], Kamdoum Tchouatchou Salomon Gloire[1]

[1]Department of Geology, University of Buea, Cameroon

[2] National Advanced school of Mines and Petroleum Industries, University of Maroua, Kaele Cameroon

Corresponding Author: jndema2012@gmail.com

To cite: Ndema et al. (2026). Petrogenetic characterization of banded iron formations of the Nyong Complex, Southern Cameroon: implications for the origin and depositional setting of Paleoproterozoic Iron Formations. Journal of Tertiary and Industrial Sciences (JTIS), 6(3), 1–47. https://doi.org/10.5281/zenodo.22179042

Submission Date: 17/05/2026 **Acceptance Date: 28/07/2026**

Abstract

Field mapping was carried out in the Bidjouka area and representative banded iron formation (BIF) samples analyzed using ICP-MS and INAA techniques. The objective of this work was to characterize the BIFs and constrain their petrogenesis, origin, evolution and depositional setting. BIFs display microband and mesoband texture, granoblastic microstructures, and are composed of biotite, quartz, and magnetite/hematite. They show 41.86-56.49 wt.% Fe_2O_3 and 39.81-49.51 wt.% SiO_2 characterizing oxide facies BIFs. The deposit shows weakly negative Eu anomaly (Eu/Eu* = 0.66-0.87) implying the signature of hydrothermal fluids (< 0.1%). BIFs have a chemogenic nature, formed in the Precambrian under different oceanic chemical conditions, and less affected by continental crustal sediments. Fe was derived from hydrothermal fluids released into the deep-ocean and the depositional site was more distal. This is a low-grade siliceous BIF, acceptable for commercial iron ores. The Bidjouka BIF deposit is mostly similar with Paleoproterozoic global BIF of Superior-type.

Keywords- Bidjouka, Microband and mesoband, Chemogenic, Low-grade, Low-T hydrothermal.

1. Introduction

Banded Iron Formations (BIFs) or Iron Formations (IFs) and iron-rich chemical sedimentary rocks refer to submarine volcanogenic exhalative chemical sediments originated in marine environment and which have precipitated in the Precambrian Ocean. BIFs are thinly banded or laminated rocks that contain > 15 wt% Fe_2O_3 and composed of intercalated microcrystalline quartz, iron oxides, silicates

Journal of Tertiary and Industrial Sciences *Vol. 6, No. 3, 2026*
ISSN 2709-3409 (Online)

and carbonates (Basta et al., 2011; Cox et al., 2013). Typical BIFs consist of alternating Si- and Fe-rich layers containing 43–56 wt.% Si and 20–40 wt.% total Fe for the low-grade iron deposits (Klein 2005; Planavsky et al., 2010). The main characteristic of BIFs is the concentration of iron (Fe) compared to low content of Al_2O_3, CaO, TiO_2, Na_2O and K_2O. Some carbonate BIFs (with CaO ≥ MgO) and alkalized silicate BIFs contain higher Na_2O content relative to K_2O. This may exceed 60 wt.% Fe in the high-grade iron ore due to secondary processes such as supergene and hypogene enrichment (Beuke et al., 2003; Hagemann et al., 2016; Braga et al., 2023). The formation and transformation of BIF to high-grade iron ore involves the processes of diagenesis, metamorphism, weathering, dissolution, precipitation and hydrothermal enrichment.

BIFs distinguish Superior, Algoma, and Rapitan types (Huston and Logan, 2004; Klein, 2005; Bekker et al., 2010; Li et al., 2014; Planavsky et al., 2014), and are characterized by silicate, carbonate, and oxide facies BIFs.

The deposition of BIF in the Archean ocean is initiated by the oxidation of dissolved iron into ferric primary precursor phases that descended through the water column and were deposited on the seafloor. Iron precipitation in BIF is initiated by the oxidation of upwelled hydrothermally supplied Fe^{2+}, either abiotically by O_2 produced by cyanobacteria (Cloud, 1973, Ohmoto et al., 2006) or by anoxygenic iron oxidizing bacteria (Kappler et al., 2005). These earlier genetic models showed that ferric oxyhydroxides are the primary precursor phases forming in the environments (Kurzweil et al., 2015). Recent models indicate that the primary precursors to BIFs formed before the Great Oxidation Event (GOE) or in deep marine volcanic settings, have consisted of mixed-valence or completely ferrous bearing phases (Li et al., 2017; Johnson et al., 2018; Koeksoy et al., 2019; Hinz et al., 2021; Sun et al., 2022). It is largely accepted that the deposition of BIF is linked to the environmental, biospheric and geochemical evolution of the Earth (Bekker et al., 2004; 2010; Cloud 1973; Tang and Chen, 2013).

BIFs are associated with Archean to Paleoproterozoic volcano-sedimentary sequences in greenstone belts related with back-arc (intra-arc basin) setting. BIF deposits in Africa, are mostly reported in the Precambrian terranes and the narrow greenstone belts around them (Ganno et al., 2017; Tamehe et al., 2018). They occurred in Ghana, Burkina, and in the northwestern margin of the Congo Craton which extends from south Cameroon, north Gabon, and northwestern Republic of Congo. In South Cameroon, BIFs constitute an important part of the Archaean to Lower Proterozoic greenstone belts (Ganno et al., 2015). Cameroon BIFs lack modern integration studies of age, lithogeochemistry, and alteration mineralogy. Microstructure and gold mineralization have made BIFs in Ghana, Burkina and Gabon viable exploration targets.

Regionally, BIFs were deposited in the Congo Craton (CC) and other super crustal volcanic and/or sedimentary sequences of deep marine environments. The north west border of the CC extends from Cameroon through north Gabon to the northwestern of the Republic of Congo, where many iron deposits were found within the Precambrian terranes and the greenstone belts (Suh et al., 2008; Ganno

Journal of Tertiary and Industrial Sciences *Vol. 6, No. 3, 2026*
ISSN 2709-3409 (Online)

et al., 2017; Tamehe et al., 2018; Ndema and Aroke, 2020; Ndema and Luku, 2020; Ndema and Mbonjoh, 2020). These cratonic regions include greenstone belts which, consist of Archean-Paleoproterozoic BIFs interbedded with volcanic rocks. IFs occurs in South Cameroon (Ntem Complex), North Gabon, and Republic of Congo (Tamehe et al., 2018; Ebotehouna et al., 2021a; Iglesias-Martínez, 2023). These IFs include granular iron formation, magnetite quartzite, magnetite gneiss and magnetite-rich calc-silicate skarn and BIFs. The Ntem Complex in South Cameroon comprises Neoarchean–Mesoarchean BIFs associated with volcanic and sedimentary rocks (Lerouge et al., 2006; Ndime et al., 2019; Nzepang et al., 2020; Ndema and Aroke, 2020; Ndema and Luku, 2020; Ndema and Mbonjoh, 2020; Tamehe et al., 2021, Djoukouo et al., 2021; Kouayep et al., 2024).

The northwestern extension of the Congo Craton in Cameroon also called Ntem Complex (Maurizot et al., 1986) hosts significant iron deposits (Mbalam, Elom, Nkout, Meyomessi, Metzimevin, Anyouzok, Toko-Nlokeng, Kouambo, Pout Njouma, Messondo, Gouap, Bikoula, Mamelles, Bibole, Kpwa-Atog Boga, Bipindi, Zambi, Bateka). The literature on the Ntem Complex iron deposits characterizes the origin and geodynamic environment of BIF, their depositional settings and some geochronological studies. However, there is no work with respect to the newly discovered Fe deposits of Bidjouka in the Nyong Complex. The Bidjouka BIF is unique within Cameroon because it represents the first documented Superior-type Paleoproterozoic banded iron formation in the Nyong Complex. Strategically, its location in the South region and its amenability to pellet production make it a distinct iron ore target for supplying regional and potentially green-steel markets. This study presents the first integrated geochemical and preliminary beneficiation assessment of the Bidjouka BIF in the Nyong Complex. The BIF of the Bidjouka is differs from Nkout, Mbalam, Gouap, Bibole, etc, because its data reveal a Superior-type BIF formed in a passive margin setting with moderate detrital input. This work provides the first evidence that Paleoproterozoic BIFs in Cameroon represent a viable, large-tonnage iron resource type distinct from the high-grade direct shipping ore (DSO) deposits of Mbalam. This study contributes genuinely new information on the Bidjouka as follows: (i) Geochemical characterization of a BIF in the Nyong Complex, revealing a Superior-type BIF with moderate detrital input, (ii) new tectonic interpretation indicating deposition in a Paleoproterozoic passive margin setting, (iii) metallurgical-geological assessment showing the BIF has simple quartz-magnetite/hematite ± biotite mineralogy amenable to conventional beneficiation, (iv) establishment of a new iron ore type for Cameroon. The Bidjouka BIF is significant because it represents the first documented Superior-type BIF in the Nyong Complex with defined geochemistry and processing potential. The main objective of this work is to characterize IFs, constrain their petrogenesis, origin and evolution, and depositional setting. The research objectives are as follows: (i) characterize the geology and geochemistry of the Bidjouka BIF, (ii) constrain it depositional environment and tectonic setting, (iii) compare it with word-class BIF deposits, and (iv) assess its preliminary mining and beneficiation.

Journal of Tertiary and Industrial Sciences *Vol. 6, No. 3, 2026*
ISSN 2709-3409 (Online)

2. Geological setting

The Congo Craton (CC) encompasses an Archean crust, early to middle Proterozoic fold belt and a Proterozoic cover (Feybesse et al., 1998). The Ntem Complex which occurs in South Cameroon (Fig. 1) refers to the North west extension of the Archean Congo Craton (ACC) and consists of three main tectonic units (Owona et al., 2020; Toteu et al., 2022): (i) The Ntem Complex in the southeast part represents the old domains of the ACC in Cameroon and it is formed between 3004 Ma and 2880 Ma (Thiéblemont et al., 2018). This complex comprises high-grade metamorphic hypersthene gneisses, trondhjemite-tonalite-granodiorite (TTG) suite emplaced at 2900 Ma, and granitic intrusions (Toteu et al., 1994). Late K-rich granitoids (2700-2500 Ma) intrude the plutonic igneous rocks and contain 3.1 Ga xenoliths of supracrustal materials which refer to the relicts of greenstone belts (Tchameni et al., 2004). The recent studies indicate that the multi-stage magmatism and the crustal growth events in the ACC came about 3750–3310 Ma, 3260–3000 Ma, 2.92–2850 Ma and 2750–2720 Ga from Eo- to Neoarchean (Akame et al., 2023).

The Ntem Complex has undergone a granulite and amphibolite metamorphism (T = 737 ± 50°C; Tchameni et al., 2010): the granulite metamorphism yields 2900 Ma while the amphibolite metamorphism is Paleoproterozoic in age (~2050 Ma: Toteu et al., 1994). The migmatization occurs at 2.843 ± 7 Ga and the second anatexis (2744 ± 31 Ma) is contemporaneous with the second phase of deformation D_2 (Akame et al., 2020a). The Ntem Complex evidenced two episodes of deformation (D_1 and D_2), and a late D_3 (2100 – 2000 Ma) phase (Owona et al., 2020). The subvertical foliation which, occurred during the high-grade metamorphic facies characterizes the D_1 deformation (Akame et al., 2020b). Isoclinal folds (F_2) and ductile shear zones (C_2) underline the second phase. The Greenstone Belts Formations older than 3.0 Ga overlay the gneisses (Caen-Vachette et al., 1988). These formations include banded siliceous and ferruginous metasedimentary rocks (BIF), aluminous metasediments, and basic to ultrabasic rocks. (ii) The Nyong Complex contains the present study area (Fig. 1) and situated in the northwest border of the Ntem Complex (Evina et al., 2023; Ndema et al., 2022a; 2025).

Journal of Tertiary and Industrial Sciences *Vol. 6, No. 3, 2026*
ISSN 2709-3409 (Online)

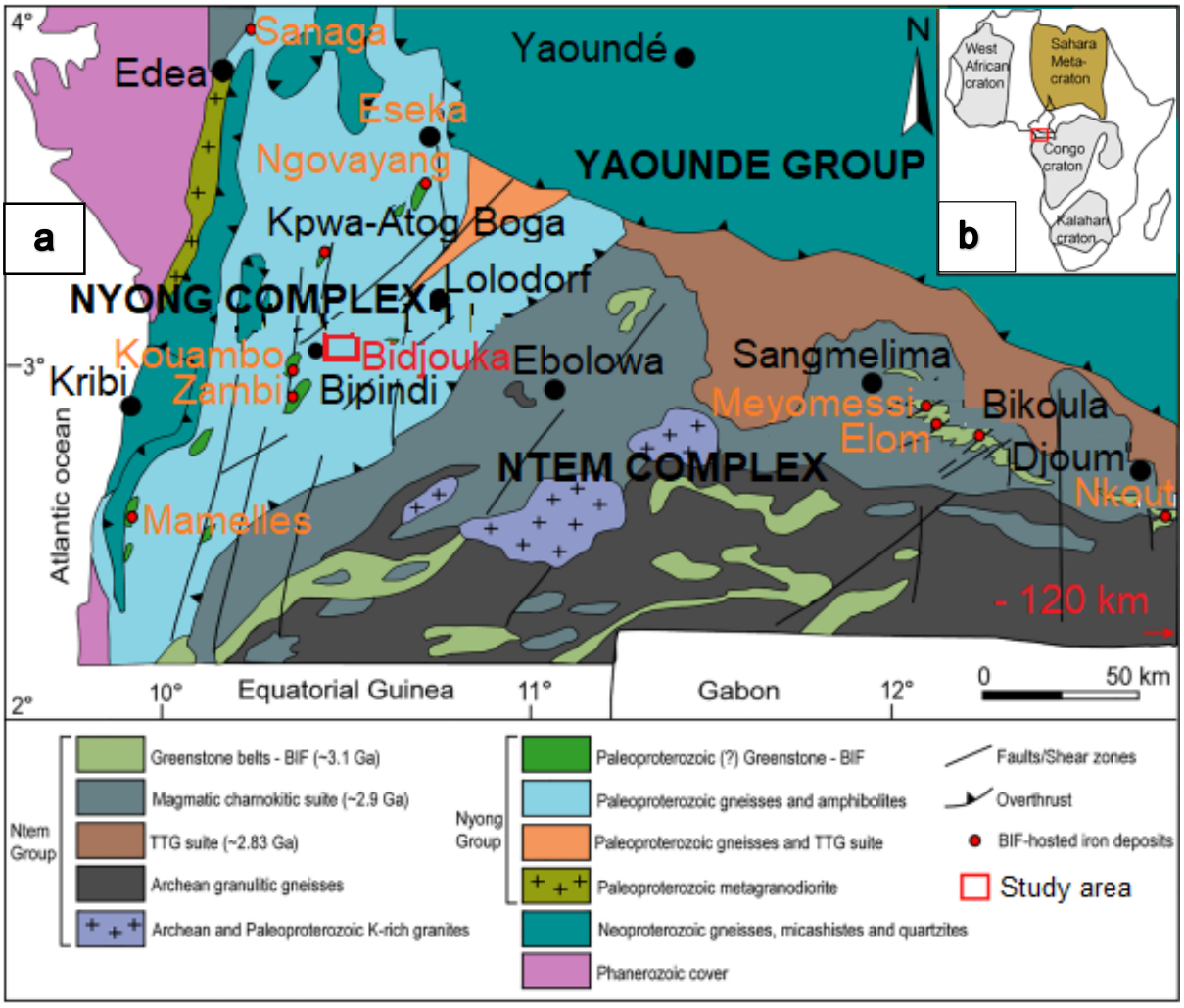

Figure.1. (a) Geological map of SW Cameroon (Maurizot et al., 1986) showing the location of the study area and (b) general view of Africa with Cameroon marked.

The Nyong Complex thrusted onto the Ntem Complex and was formed during the Paleoproterozoic. Metamorphism and deformation in this complex occur during the Eburnean or Paleoproterozoic Orogeny (Owona et al., 2022; Ndema et al., 2025). The Nyong Complex includes metasedimentary and metavolcanic rocks, granitoids and syenites (Pouclet et al., 2007; Ndema et al., 2014). Intrusions of metadiorites, granodiorites, syenites and post-tectonic dolerites also characterize the Nyong Complex (Lerouge et al., 2006). The age of deposition ranges from 2400 to 2200 Ma and four main groups of rocks identified (Owona et al., 2021): the first group includes metavolcanic sedimentary rocks made up of remnants of greenstone belts. Metavolcanic rocks emplaced at 2.671 ± 51 Ga and metamorphism occurred at 2065 ± 55 Ma (Mvodo et al., 2022). The second group is made up of migmatitic grey gneiss of TTG composition. The third group of rock consists of granitoids, charnockite, syenite, gneiss. The

Journal of Tertiary and Industrial Sciences *Vol. 6, No. 3, 2026*
ISSN 2709-3409 (Online)

precursors to the gneisses were derived from 2.9 Ga Archaean rocks and document the existence of a major high-grade metamorphic event (2.1-2.0 Ga), responsible for the migmatization (Feybesse et al., 1987; Van Schmus and Toteu, 1992). The migmatization is linked to the Eburnean orogeny and late Pan-African events. The fourth group encompasses the meta-dolerites (Owona et al., 2012). In this Complex, IFs include both granular iron formations (GIFs) and BIFs, contrary to Nkout situated in the Ntem Complex in which only BIFs occur. The Nyong Complex experienced a polyphase deformation (Ndema et al., 2019; 2022a). The High-grade metamorphism is contemporaneous with the tectonic emplacement of plutonites (Owona et al., 2020; Lerouge et al., 2006; Ndema et al., 2022a; Ndema et al., 2025). (iii) The Pan-African Fold Belt (Fig. 1) results from the Neoproterozoic collision between the Congo, West African, and Saharan shields (Caxito et al., 2020). The Yaoundé Group represents the Pan-African Fold Belt in Cameroon (Ngnotué et al., 2012) and includes a huge nappe that thrusts in the south toward the Ntem complex and composes of Neoproterozoic metasedimentary rocks.

The tectonic-stratigraphy section shows that the IFs yield Paleoproterozoic ages (1500–2600 Ma) associated with Paleoproterozoic or Eburnean orogeny (Fig. 2). In Cameroon, the Paleoproterozoic orogeny has affected the Nyong Complex (Lerouge et al., 2006; Owona et al., 2022), meanwhile the Ntem Complex also evidenced some Paleoproterozoic materials (Toteu et al., 1994; Tchameni et al., 2001; Kouayep et al., 2024).

The newly discovered iron ore deposit of Bidjouka is found within the Bipindi iron ore district located within the central part of the Nyong Complex in Cameroon (Fig. 1). The local geologic map showing the position of the selected IFs samples is presented in Fig. 3. The Bipindi iron ore district comprises Mewongo, Bibole, Kouambo, Zambi, Gouap, and BIFs (Ganno et al., 2017; Ndema and Mbonjoh, 2020; Djoukouo et al., 2021; Tamehe et al., 2018; 2024). The Bidjouka area which hosts the newly discovered BIFs of this iron district is made up of gneiss, amphibolite and TTG (Maurizot et al., 1986). Gneisses are composed of fine- grained gneiss, orthopyroxene gneiss, biotite- hornblende gneiss, garnet- gneiss and charnockitic gneiss. Amphibolites occur as discontinuous bands while TTGs outcrop as diffuse pegmatitic veins. Garnet- rich metabasite of the Ngovayang massif occur westward and north western part of the Bidjouka area. More recently, gold mineralization was recorded within the placer deposits of Bidjouka area (Ndema et al., 2024). These sediments originated from metamorphic sources and were deposited under humid, oxic and oxidizing conditions during weathering processes (Ndema et al., 2024). In the gneiss of the Ngovayang massif, the S_1 regional foliation is oriented ENE-WSW and underlined by a compositional banding make by alternating lithological layers. The pre- D_1 deformational phase is characterized by isoclinal folds showing axial plane schistosity. All these rocks were metamorphosed under amphibolite and granulite metamorphic facies conditions. The local geologic map showing the position of the selected samples indicates that greenstone belts are the host rocks of IFs (Fig. 3).

Journal of Tertiary and Industrial Sciences *Vol. 6, No. 3, 2026*
ISSN 2709-3409 (Online)

Cycle and age (Ma)	Lithology		Major tectonic events	Stratigraphic formation
Phanerozoic		**Phanerozoic cover**		
550				
Pan-African		**Pan-African orogeny** ↑ Metamorphism Gneiss/migmatite amphibolite/schist	**D_1 deformation** - Foliation S_{0-1} - F_1 folding **D_2 deformation** - Tectonic nappe - Migmatisation **D_3 deformation** Fault, joint	Poli and Lom Series Yaounde Group Yokadouma Series
1000				
1600		**Paleoproterozoic orogeny(Eburnean)** ↑ Metamorphism Charnockite/TTG/gneiss/syenite Greenstone belt Iron formation (IF)/schist/quartzite/amphibolite/dolerite dyke/eclogite	**D_1 deformation** - Foliation S_{0-1} **D_2 deformation** - Foliation S_2 - L_2 Lineation - F_2 folding - Shear band cleavage - Strike slip fault	Nyong Complex
Paleoproterozoic				
2500				
Liberian (Archean)		**Liberian orogeny** ↑ Metamorphism High-k granite/dyke ↑ Migmatite TTG/charnockite ↑ Paleoarchean crust	**S_1 deformation** Liberaian foliation S_1	Ntem Complex
2900				

Figure 2. Tectono-stratigraphic column with the IF position for different units.

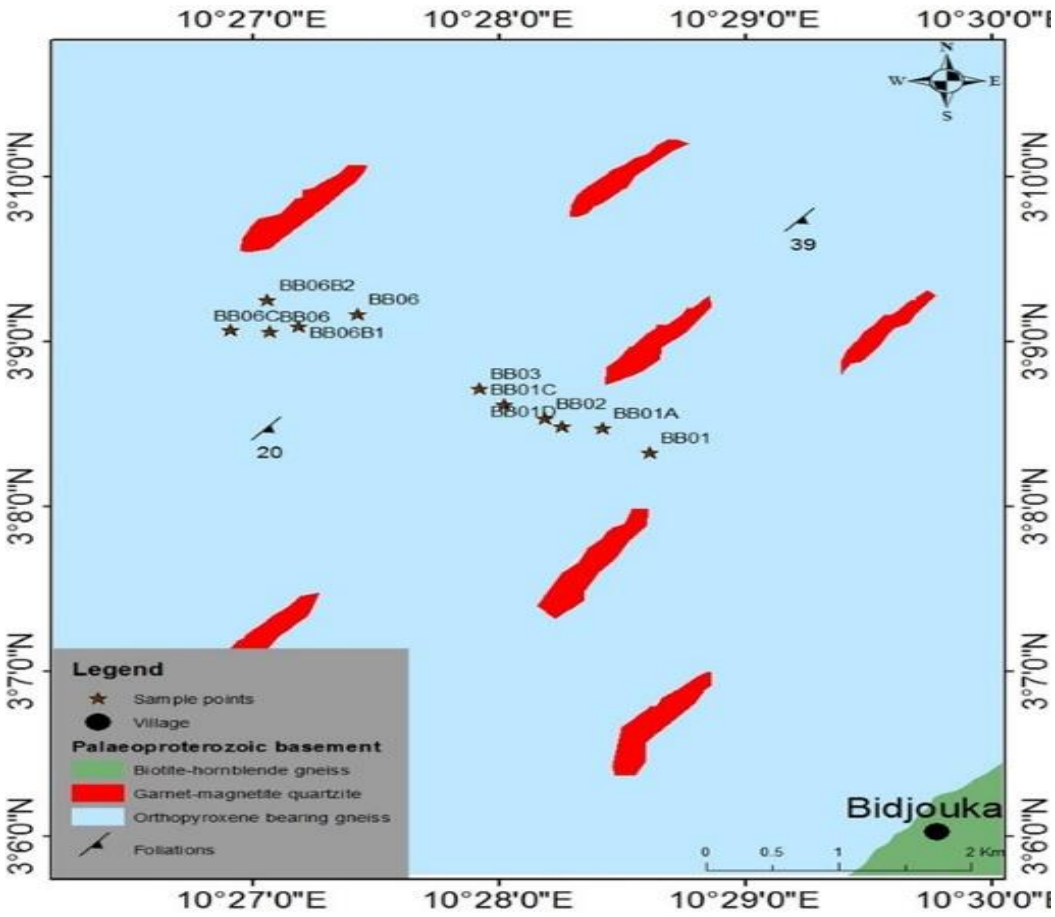

Journal of Tertiary and Industrial Sciences *Vol. 6, No. 3, 2026*
ISSN 2709-3409 (Online)

Figure 3. Local geology map with the position of the selected samples.

3. Methods of investigation

The field work consisted in mapping the study area and collection of rock samples. During field work, we have collected fifteen (15) BIF samples based on their magnetic properties. Six (06) thin sections among representative rock samples collected were made in Yaoundé at the Laboratory of the Institute of Geological Research and Mining (IGRM), followed with their observation in the Geologic Laboratory at the Department of Geology, University of Buea under a polarizer microscope for petrographic studies. Geochemical analysis (major, trace and rare earth elements) was carried out on nine (09) representative samples of BIF at Activation Laboratories (ACTLABS) in Canada using inductively coupled plasma (ICP) and instrumental neutron activation analysis (INAA).

3.1. INAA measurements

The samples were weighed and encapsulated in a polyethylene via and irradiated along with flux wires at a thermal neutron flux of 7 x 10^{12} n/cm^2/s. After a 7-day period, to allow ^{24}Na to decay, the samples are counted on a high purity germanium (HPGe) detector with a resolution better than 1.7 keV at the 1332 keV ^{60}Co photopeak. Using the flux wires and control standard, the decay-corrected activities are compared to a calibration developed from multiple certified international reference materials. One blank is analyzed per work order and duplicate samples are also analyzed.

3.2. ICP measurements

A sample of 0.25 gram is digested with four acids starting with hydrofluoric, then followed by a mixture of nitric and perchloric acids. This is then heated using precise programmer-controlled heating in several ramping and holding cycles which takes the samples to incipient dryness is attained, samples are brought back to the solution. The sample are then analyzed using an ICP. The analytical precision for major oxides and trace elements were 1-3% relative standard deviation (RSD) for ICP methods. The precision of gamma-counted to determine Au, As, Sb, Co, rare earth elements (REEs), and other pathfinder elements were 1-5% RSD for the INAA methods. Quality control (QC) for the digestion is 14% for each batch, 5 method reagent blanks, 10 samples duplicates and 8 certified reference materials. An additional 13% QC were performed as part of the instrumental analysis to ensure quality in the areas of instrumental drift. The QC results are presented in Table 1.
Major geochemical like SiO_2, Al_2O_3, $Fe_2O_{3(T)}$, MgO, CaO, Na_2O, K_2O, P_2O_5, and Total were analyzed with the detection limit (DL) of 0.01 %. The DL for TiO_2 and SO_3 is 0.005 and 0.001%, respectively. The DL of trace elements shows 0.5 ppm for Ag, Cd, Cs, Hf, Th, and U. Elements such as As, Bi, Mo, Sr, Zr have the DL of 2 ppm, 5 ppm for Au, Ir, Pb, and V, 3 ppm for Ba, Se, and W. Elements including Be,

Journal of Tertiary and Industrial Sciences *Vol. 6, No. 3, 2026*
ISSN 2709-3409 (Online)

Br, Co, Cr, Cu, Hg, Ni, Ta, Y, and Zn were determined with the DL of 1 ppm. The other trace elements such as Mn, Rb, Sb, and Sc were quantified with the DL of 0.01, 20, 0.2 and 0.1 ppm, respectively. Rare earth elements (REEs) like La, Ce, Nd, Tb, and Lu were analyzed with the DL of 0.2, 3, 5, 0.5, and 0.05 ppm, respectively while the DL of Sm, Eu, and were 0.1 ppm. Loss of ignition (LOI) was obtained by gravimetry (GRAV). The following relation has served to determine the detrital input:

$$\% \text{ detritus} = 100 \times (X_{sample}/X_{MQS}), \quad (2)$$

in which Xsample refers to Al_2O_3 in the analyzed IF and X_{MQS} = 17.3% denotes the average Al_2O_3 in the muscovite–quartz schist. Since we have not analyzed some rare earth elements (eg., Pr, Gd, Dy, Ho, Er, Tm), the expression of Eu/Eu* and Ce/Ce* anomalies respect the equations:

$$Eu/Eu^* = Eu_{PASS}/(0.67Sm_{PAAS} + 0.33Tb_{PAAS}) \text{ by Bau and Dulski (1996)} \quad (3)$$

$$\text{and } Ce/Ce^* = Ce_{PAAS}/(La_{PAAS} \times Nd_{PAAS})^{1/2} \text{ by Akagi and Masuda (1998).} \quad (4)$$

Rare earth elements were normalized with post-Archean shales from Australia (PAAS) by McLennan (1989), and trace elements by Taylor and McLennan (1985).

4. Results

4.1 Petrography

The Bidjouka BIFs outcrop in-situ (Fig. 4a, b), as sub-outcrop (5 to 7 m in diameter) and boulders of various sizes (2-5 m). Smaller dismantled blocks with variable sizes (10-30 cm) also occurred in the study area. The BIFs are moderately to strongly magnetic, most samples are highly weathered and display a yellow-brownish coloration (Fig. 4c). They are massive (Fig. 4d), laminated (Fig. 4a) and foliated (Fig. 4c). Two elements characterize the foliation: (i) the alternation of light and dark layers with light layers showing quartz or silica enrichment while dark layers consist of magnetite and/or hematite mostly (Fig. 4c), (ii) S_1 schistosity underlined by a preferred orientation of stretched quartz and magnetite and/or hematite crystals. In hand specimen, the IF samples and display alternating magnetite and/or hematite- rich layers and quartz- rich layers showing mesoband and microband texture. At outcrop scale, the microband and mesoband texture consist of small-scale (millimetric to centimetric) lamination (Fig. 4a). The host rocks show a compositional banding marked by alternating of light and dark bands. The light bands show quartz minerals, while dark bands show enrichment in ferromagnesian minerals such as biotite and magnetite/hematite.

In the polarizing microscope, the Bidjouka BIF samples are made up of intercalated silica-rich light minerals and magnetite and/or hematite- rich layers, and show granoblastic microstructure define by the millimetric to micrometric scale textures, quartz + magnetite/hematite ± biotite mineral assemblage, and a S_1 foliation. The minerals present include iron oxide (magnetite and/or hematite), quartz and biotite (Fig. 2e, f). Iron oxide contributes 40 vol.% of the rock and appears as monocrystalline ribbon displaying subhedral shape, and oriented following S_1 foliation. Some iron

Journal of Tertiary and Industrial Sciences *Vol. 6, No. 3, 2026*
ISSN 2709-3409 (Online)

oxide crystals contain biotite and quartz as inclusion showing a prefer orientation that underline an internal fabric, Si schistosity. Quartz (45 vol.%) occurs as polycrystalline bands with anhedral shape displaying undulose extinction, and frequently associated with iron oxide. Biotite (2 vol.%) occurs as disseminated crystals and oriented, and in association with iron oxide and quartz (Fig. 2f).

Journal of Tertiary and Industrial Sciences *Vol. 6, No. 3, 2026*
ISSN 2709-3409 (Online)

Table 1. Results of quality control

Analyte symbol	SiO_2	Al_2O_3	$Fe_2O_{3(T)}$	MgO	CaO	Na_2O	K_2O	TiO_2	P_2O_5	SO_3	Total	Au	Ag	Ag	As	Ba
Analysis method	FUS-ICP	FUS-ICP	FUS-ICP	FUS-ICP	FUS-ICP	FUS-ICP	FUS-ICP	FUS-ICP	FUS-ICP	FUS-ICP	FUS-ICP	INAA	TD-ICP	INAA	INAA	FUS-ICP
Detection limit	0.01	0.01	0.01	0.01	0.01	0.01	0.01	0.005	0.01	0.001	0.01	5	0.5	5	2	2
DNC-1 Meas	47.07	18.48	9.89	10.12	11.33	1.91	0.22	0.483	0.03							107
DNC-1 Cert	47.15	18.34	9.97	10.13	11.49	1.89	0.234	0.48	0.07							118
SY-4 Meas	49.76	20.48	6.1	0.5	7.99	6.9	1.65	0.28	0.1							349
SY-4 Cert	49.9	20.69	6.21	0.54	8.05	7.1	1.66	0.287	0.131							340
BIR-1a Meas	47.76	15.59	11.21	9.59	13.28	1.81	0.02	0.966	< 0.01							7
BIR-1a Cert	47.96	15.5	11.3	9.7	13.3	1.82	0.03	0.96	0.021							6
OREAS 101b (4 Acid) Meas																
OREAS 101b (4 Acid) Cert																
OREAS 904 (4 Acid) Meas										0.06			0.5			
OREAS 904 (4 Acid) Cert										0.063			0.55			
OREAS 45d (4-Acid) Meas										0.045						
OREAS 45d (4-Acid) Cert										0.049						
OREAS 905 (INAA) Meas												387			35	
OREAS 905 (INAA) Cert												391			36	
W-2b Meas	52.81	15.53	10.88	6.35	10.95	2.25	0.62	1.093	0.09							180
W-2b Cert	52.4	15.4	10.7	6.37	10.9	2.14	0.626	1.06	0.14							182
OREAS 620 (4 Acid) Meas										2.44			39.8			
OREAS 620 (4 Acid) Cert										2.47			38.5			
BBO6 Orig										0.003			< 0.5			
BBO6 Dup										0.003			< 0.5			
BBO6B1 Orig	40.4	2.45	53.76	1.91	0.67	0.06	0.08	0.263	0.46		100.1					10
BBO6B1 Dup	39.21	2.5	54.82	1.86	0.65	0.02	0.01	0.229	0.46		99.75					10
Method Blank										< 0.001			< 0.5			
Method Blank										< 0.001			< 0.5			
Method Blank	0.01	< 0.01	< 0.01	< 0.01	< 0.01	< 0.01	< 0.01	< 0.005	< 0.01							< 2

Journal of Tertiary and Industrial Sciences *Vol. 6, No. 3, 2026*
ISSN 2709-3409 (Online)

Method Blank														< 5		< 5	< 2	
Method Blank	0.01	< 0.01	< 0.01		< 0.01	< 0.01	< 0.01	< 0.01	< 0.005	< 0.01								< 2

Analyte symbol	Ba	Be	Bi	Br	Cd	Co	Cr	Mn	Cs	Cu	Hf	Hg	Ir	Mo	Ni	Pb	Rb	Sb
Analysis method	INAA	FUS-ICP	TD-ICP	INAA	TD-ICP	INAA	INAA	INAA	TD-ICP	INAA	INAA	INAA	TD-ICP	TD-ICP	TD-ICP	INAA	TD-ICP	INAA
Detection limit	50	1	2	1	0.5	1	1	0.01	0.5	1	0.5	1	5	2	1	5	20	0.2
DNC-1 Meas								0.14										
DNC-1 Cert								0.15										
SY-4 Meas		3						0.11										
SY-4 Cert		2.6						0.108										
BIR-1a Meas		< 1						0.17										
BIR-1a Cert		0.58						0.175										
OREAS 101b (4 Acid) Meas										399				21	8	23		
OREAS 101b (4 Acid) Cert										412				20	8.2	23		
OREAS 904 (4 Acid) Meas			5							5950				< 2	44	11		
OREAS 904 (4 Acid) Cert			4.05							6120				2.1	40	10.6		
OREAS 45d (4-Acid) Meas			< 2							366				< 2	229	22		
OREAS 45d (4-Acid) Cert			0.31							371				2.5	231	21.8		
OREAS 905 (INAA) Meas	2380					14			7.7		6.6						110	1.9
OREAS 905 (INAA) Cert	2800					15.3			7.1		7.26						137	1.96
W-2b Meas		< 1						0.16										
W-2b Cert		1.3						0.163										
OREAS 620 (4 Acid) Meas			< 2		166					1690				9	15	> 5000		
OREAS 620 (4 Acid) Cert			2		163					1730				9	15	7740		
BBO6 Orig			3		0.7					9				< 2	92	10		
BBO6 Dup			< 2		0.6					8				< 2	91	10		
BBO6B1 Orig		< 1						0.04										
BBO6B1 Dup		< 1						0.04										

Journal of Tertiary and Industrial Sciences *Vol. 6, No. 3, 2026*
ISSN 2709-3409 (Online)

Method Blank				< 2		< 0.5					< 1				< 2	< 1	< 5		
Method Blank				< 2		< 0.5					< 1				< 2	< 1	< 5		
Method Blank			< 1						< 0.01										
Method Blank		< 50			< 1		< 1	< 1		< 0.5		< 0.5	< 1	< 5				< 20	< 0.2
Method Blank			< 1						< 0.01										

Analyte symbol	Sc	Se	Sr	Ta	Th	U	V	W	Y	Zn	Zr	La	Ce	Nd	Sm	Eu	Tb	Yb	Lu
Analysis method	INAA	INAA	FUS-ICP	INAA	INAA	INAA	FUS-ICP	INAA	FUS-ICP	TD-ICP	FUS-ICP	INAA	INAA	INAA	INAA	INAA	INAA	INAA	INAA
Detection limit	0.1	3	2	1	0.5	0.5	5	3	1	1	2	0.2	3	5	0.1	0.1	0.5	0.1	0.05
DNC-1 Meas			146				149		17		37								
DNC-1 Cert			144				148		18		38								
SY-4 Meas			1175				6		125		549								
SY-4 Cert			1191				8		119		517								
BIR-1a Meas			110				318		15		16								
BIR-1a Cert			110				310		16		18								
OREAS 101b (4 Acid) Meas																			
OREAS 101b (4 Acid) Cert																			
OREAS 904 (4 Acid) Meas										29									
OREAS 904 (4 Acid) Cert										26.3									
OREAS 45d (4-Acid) Meas										44									
OREAS 45d (4-Acid) Cert										45.7									
OREAS 905 (INAA) Meas				< 1	14.4	4.8		< 3				49.2	96	51	7.3	1.4	< 0.5	< 0.1	
OREAS 905 (INAA) Cert				1.38	14.7	5		3.02				48	96	41	7.6	1.46	0.81	0.76	
W-2b Meas			199				267		21		96								
W-2b Cert			190				262		24		94								
OREAS 620 (4 Acid) Meas										> 10000									
OREAS 620 (4 Acid) Cert										31500									
BBO6 Orig										66									

Journal of Tertiary and Industrial Sciences *Vol. 6, No. 3, 2026*
ISSN 2709-3409 (Online)

BBO6 Dup										69									
BBO6B1 Orig			12			27		13		100									
BBO6B1 Dup			13			27		12		96									
Method Blank										< 1									
Method Blank										< 1									
Method Blank			< 2			< 5		< 1		< 2									
Method Blank	< 0.1	< 3		< 1	< 0.5	< 0.5		< 3				< 0.2	< 3	< 5	< 0.1	< 0.1	< 0.5	< 0.1	< 0.05
Method Blank			< 2			< 5		< 1		< 2									

Journal of Tertiary and Industrial Sciences *Vol. 6, No. 3, 2026*
ISSN 2709-3409 (Online)

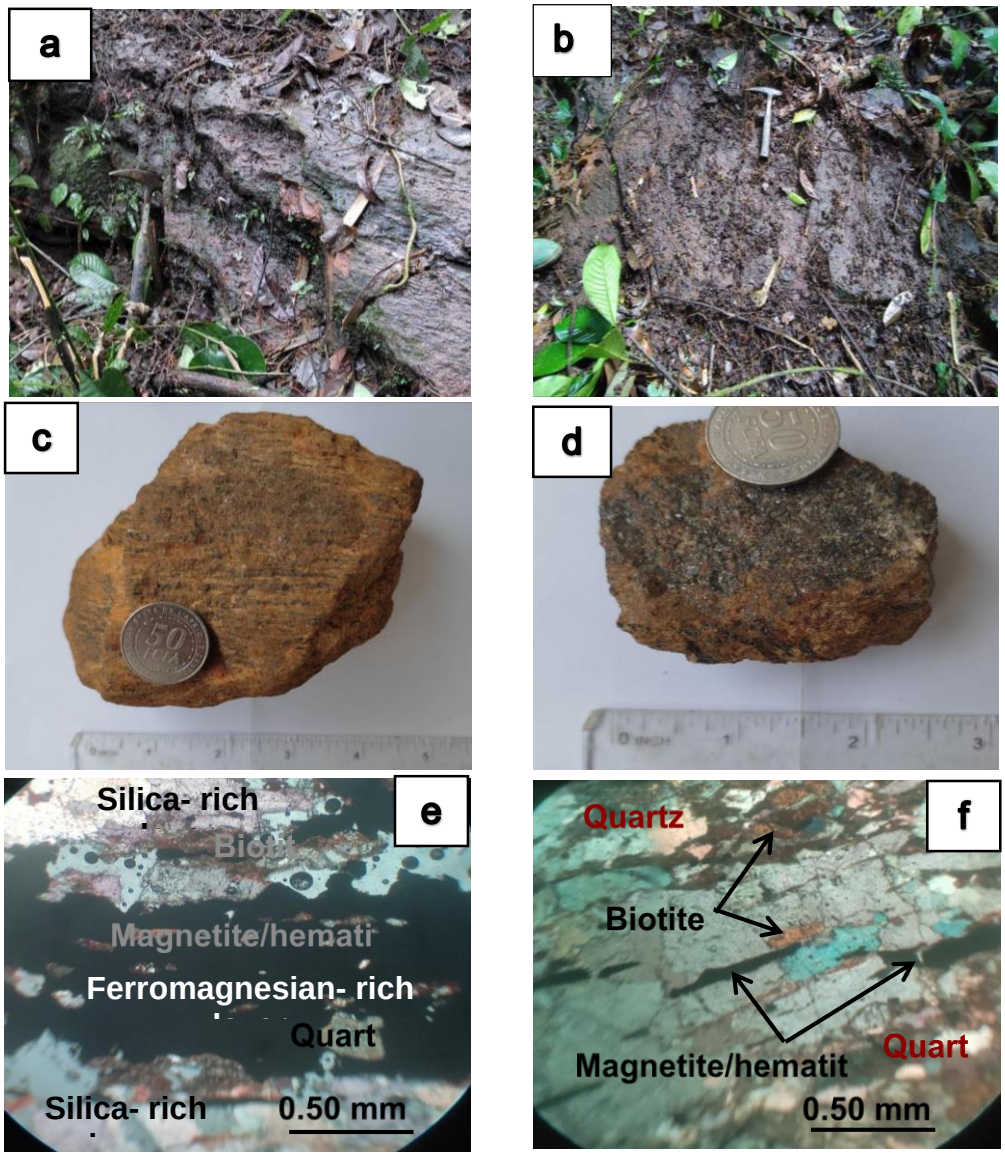

Figure 4. Bidjouka BIF occurrence. (a, b) Exposure of BIF outcrop, note the gentle dipping of the foliation and micro- and mesoband texures; (c) hand specimen picture of BIF showing mesobanding, note the yellow-brownish coloration due to weathering; (d) massive BIF sample; (e, f) microphotographs showing granoblastic microstructure and mineral composition.

4.2. Whole-rock geochemistry

4.2.1 Major oxides

Journal of Tertiary and Industrial Sciences *Vol. 6, No. 3, 2026*
ISSN 2709-3409 (Online)

The composition of major element of the analyzed Bidjouka BIFs is shown in Table 2. The whole-rock geochemistry of major oxides shows 39.81 to 49.51 wt.% SiO_2 and 41.86 to 56.49 wt.% $Fe_2O_{3(T)}$ indicating that SiO_2 (avg.: 44.99 wt.%) and Fe_2O_3 (avg.: 51.07 wt.%) are the dominant components. The content of SiO_2 and $Fe_2O_{3(T)}$ matches with the aforementioned mineralogy of the rock which a predominantly of quartz and iron oxide. Plotted in the triplot SiO_2-(Al_2O_3 + TiO_2)-Fe_2O_3 (Fig. 5a), the samples fall close to the middle of the mixing line SiO_2-Fe_2O_3, indicating enrichment in SiO_2 and depletion in immobile oxides such as Al_2O_3 (1.01-4.08 wt.%) and TiO_2 (0.07-0.47 wt.%). These BIFs are depleted in MgO (0.03-1.88 wt.%) and CaO (0.04-0.72wt. %) suggesting lack of carbonate and silicate minerals. LOI value ranges from -1.05-1.41% (Table 2) with samples BBO1A, BBO1C, BBO1D and BBO6B1 showing negative LOI values indicating they have gained weight. The total alkali content (Na_2O + K_2O) ranges from 0.04 to 0.09 wt.% and P_2O_5 concentration 0.12 to 0.54 wt.%. The concentrations of Na_2O (0.02–0.05 wt.%) and K_2O (< 0.01–0.06 wt.%) are non-insignificant. SO_3 content are in the range of 0.00–0.02 wt.%. In the TiO_2 vs SiO_2 discrimination graph (Tarney, 1977), the investigated rocks fall within the sedimentary field (Fig. 5b). Fe_2O_3 and SiO_2 (r = -0.84) exhibit a very strong negative correlation (Fig. 6; 7a). $Fe_2O_{3(T)}$ and Al_2O_3 (r = -0.80) show a negative correlation (Fig. 6; 7b), while TiO_2 and Al_2O_3 (r = 0.80; Fig. 6; 7c) display a positive correlation, and no significant correlation between P_2O_5/Fe_2O_3 and P_2O_5/SiO_2 (Fig. 7d).

Table 2**.** Geochemical element composition of the Bidjouka Banded iron formations.

Sample	DL	BBO1A	BBO1C	BBO1D	BBO2	BBO3	BBO6	BBO6B1	BBO6B2	BBO6C
SiO_2 (%)	0.01	46.60	45.06	42.78	43.99	46.66	49.51	39.81	44.33	46.14
Al_2O_3	0.01	1.04	1.03	1.01	1.93	2.73	4.08	2.47	2.35	2.38
% Detritus		6.01	5.95	5.84	11.16	15.78	23.8	14.28	13.58	13.76
$Fe_2O_{3(T)}$	0.01	50.30	54.10	56.49	52.49	49.23	41.86	54.29	50.96	49.88
MgO	0.01	1.02	0.63	0.81	1.01	0.03	1.54	1.88	1.79	0.75
CaO	0.01	0.50	0.24	0.33	0.25	0.04	0.72	0.66	0.41	0.16
Na_2O	0.01	0.05	0.03	0.03	0.02	0.03	0.03	0.04	0.02	0.02
K_2O	0.01	0.01	< 0.01	< 0.01	0.02	0.03	0.06	0.04	< 0.01	< 0.01
TiO_2	0.005	0.10	0.10	0.11	0.12	0.07	0.47	0.25	0.21	0.22
P_2O_5	0.01	0.12	0.13	0.17	0.44	0.12	0.54	0.46	0.20	0.25
SO_3	0.001	0.02	0.01	0.01	0.00	0.02	0.01	0.00	0.01	0.01
LOI		-0.95	-0.87	-1.05	0.23	1.41	0.33	-0.04	0.05	0.68
Total	0.01	98.84	99.43	99.80	99.50	99.40	99.20	99.90	99.70	99.70
Na_2O + K_2O		0.06	n.d	n.d	0.04	0.06	0.09	0.08	n.d	n.d
K_2O/Al_2O_3		0.01	n.d	n.d	0.01	0.01	0.01	0.02	n.d	n.d
Al_2O_3/TiO_2		10.95	10.40	9.62	16.64	42.00	8.72	10.04	11.14	11.07
Si/Al		44.81	43.75	42.36	22.79	17.09	12.13	16.12	18.86	19.39
Fe/Al		63.92	69.42	73.92	35.94	23.83	13.56	29.05	28.66	27.70
Ag (ppm)	0.5	< 0.5	< 0.5	< 0.5	< 0.5	< 0.5	< 0.5	< 0.5	< 0.5	< 0.5
As	2	< 2	< 2	< 2	< 2	4	< 2	< 2	< 2	< 2

Journal of Tertiary and Industrial Sciences *Vol. 6, No. 3, 2026*
ISSN 2709-3409 (Online)

Au	5	< 5	< 5	< 5	< 5	< 5	< 5	< 5	< 5	< 5
Ba	3	61	33	29	21	62	30	10	8	6
Be	1	< 1	< 1	< 1	< 1	< 1	< 1	< 1	< 1	< 1
Bi	2	3	4	3	4	4	< 2	5	4	7
Br	1	< 1	< 1	< 1	< 1	< 1	< 1	< 1	< 1	< 1
Cd	0.5	0.7	0.7	0.9	0.7	0.7	0.6	0.8	0.6	0.7
Co	1	8	7	9	6	6	15	9	9	7
Cr	1	21	20	18	42	21	92	17	20	15
Mn	0.01	0.03	0.03	0.03	0.02	0.02	0.04	0.03	0.03	0.02
Cs	0.5	1.3	< 0.5	< 0.5	< 0.5	< 0.5	< 0.5	< 0.5	< 0.5	< 0.5
Cu	1	8	9	10	8	10	9	9	9	9
Hf	0.5	< 0.5	< 0.5	< 0.5	< 0.5	1.4	< 0.5	1.4	< 0.5	< 0.5
Hg	1	< 1	< 1	< 1	< 1	< 1	< 1	< 1	< 1	< 1
Ir	5	< 5	< 5	< 5	< 5	< 5	< 5	< 5	< 5	< 5
Mo	2	< 2	< 2	< 2	< 2	< 2	< 2	< 2	< 2	< 2
Ni	1	37	36	36	18	10	91	58	54	54
Pb	5	11	12	12	12	13	10	10	11	12
Rb	20	< 20	< 20	< 20	< 20	< 20	< 20	< 20	< 20	< 20
Sb	0.2	< 0.2	< 0.2	< 0.2	< 0.2	< 0.2	< 0.2	< 0.2	< 0.2	< 0.2
Sc	0.1	1.8	1.9	1.7	2.5	2	7.5	4.1	4.5	4.1
Se	3	< 3	< 3	< 3	< 3	< 3	< 3	< 3	< 3	< 3
Sr	2	16	12	15	11	7	13	12	6	4
Ta	1	< 1	< 1	< 1	< 1	< 1	< 1	< 1	< 1	< 1
Th	0.5	< 0.5	< 0.5	< 0.5	3.1	< 0.5	3.8	2.1	0.9	1.5
U	0.5	< 0.5	< 0.5	< 0.5	< 0.5	< 0.5	< 0.5	< 0.5	< 0.5	< 0.5
V	5	9	12	12	20	23	77	27	24	28
W	3	< 3	< 3	< 3	< 3	< 3	< 3	< 3	< 3	< 3
Y	1	12	11	14	6	3	11	12	10	5
Zn	1	26	26	28	32	13	68	40	39	37
Zr	2	18	31	211	9	77	28	98	17	13
La	0.2	48.7	62.4	63.1	23.4	18.4	24.3	15.6	9.6	6.4
Ce	3	58	97	90	49	66	55	40	31	16
Nd	5	52	67	68	19	7	41	20	14	9
Sm	0.1	10	12.8	12.6	4.6	1.4	6.1	5.3	3.7	1.6
Eu	0.1	2.2	2.4	2.3	0.7	0.3	0.5	1.1	0.7	0.3
Tb	0.5	< 0.5	< 0.5	2.2	< 0.5	< 0.5	< 0.5	2.1	< 0.5	< 0.5
Yb	0.1	1.5	1.4	1.1	< 0.1	< 0.1	0.9	0.8	0.6	0.6
Lu	0.05	0.12	0.10	0.19	< 0.05	< 0.05	0.07	0.14	0.09	0.06
ΣREE		n.d	n.d	239.49	n.d	n.d	127.87	85.04	n.d	n.d
REE-Y		n.d	n.d	253.49	n.d	n.d	138.87	97.04	n.d	n.d
Sm/Yb		6.67	9.14	11.45	n.d	n.d	6.78	6.63	6.17	2.67
Eu/Sm		0.22	0.19	0.18	0.15	0.21	0.08	0.21	0.19	0.19
$(La/Yb)_N$		2.40	3.29	4.23	n.d	n.d	1.99	1.44	1.18	0.79
$(La/Sm)_N$		0.71	0.71	0.73	0.74	1.91	0.58	0.43	0.38	0.58
$(Tb/Yb)_N$		n.d	n.d	7.29	n.d	n.d	n.d	9.56	n.d	n.d
$(La/Lu)_N$		4.60	7.07	3.76	n.d	n.d	3.93	1.26	1.21	1.21

Journal of Tertiary and Industrial Sciences *Vol. 6, No. 3, 2026*
ISSN 2709-3409 (Online)

Eu/Eu*	n.d	n.d	0.87	n.d	n.d	n.d	0.66	n.d	n.d
Ce/Ce*	0.52	0.53	0.49	0.46	0.77	0.44	0.42	0.41	0.26

DL: detection limit; n.d: non determined; LOI: loss of ignition.

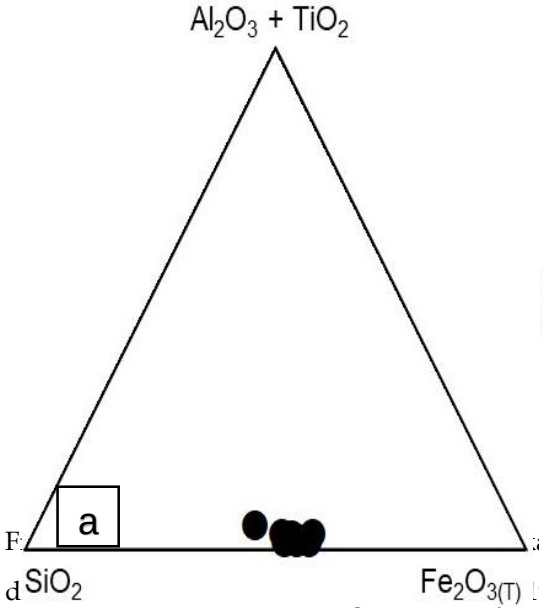

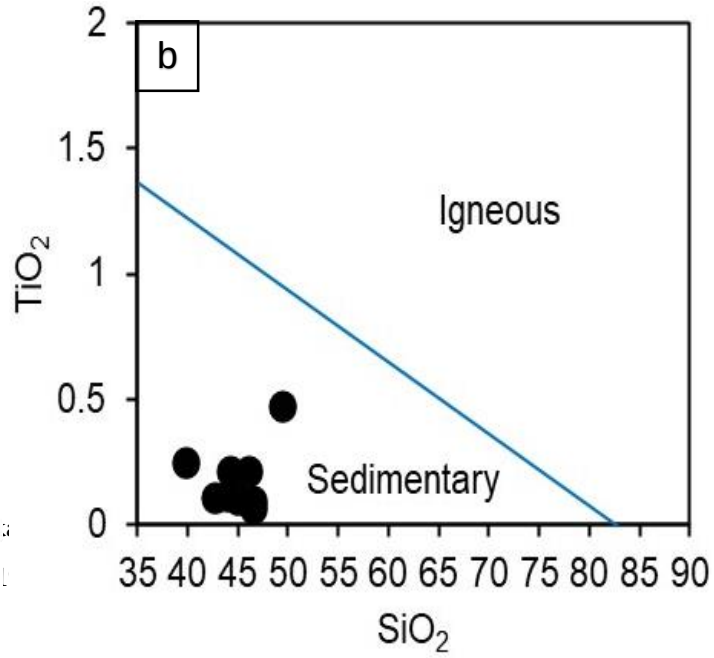

4.2.2. Trace elements

Trace element composition of the Bidjouka BIF samples is presented in Table 2. The content of large ion lithophile elements (LILE) like Pb (10–13 ppm, avg.: 11.44 ppm), Sr (4–16 ppm, avg.: 10.67 ppm), and Th (< 0.5–3.8 ppm) are relatively low compared to Ba (6 to 62 ppm, avg.: 28.89 ppm). The concentration of Rb (< 20 ppm) and U (< 0.5 ppm) are uniform in the samples. Hf (< 0.5-1.4 ppm) shows lower value compared to Zr (9-211 ppm, av: 55.78 ppm; Table 2), another high field strength elements (HFSE). Transition metals such as V (9–77 ppm), Zn (13-68 ppm), Ni (10-91ppm), Cr (15–92 ppm), and Cu (8–10 ppm) show moderate and variable contents. Fe_2O_3 show positive correlation with Cd (r = 0.75) and Zr (r = 0.51), whereas negative with Cr, Co, Ni, V, and Zn (Fig. 6). In the binary plots (Fig. 7e), Zr shows positive trend with Fe_2O_3, but its concentration decreases with Al_2O_3 (Fig. 7f). The spider diagram (Fig. 8a) for elements that exhibit numerical values shows that the investigated BIFs show depletion in trace element concentrations relative to PAAS (Taylor and McLennan 1985); except Bi (< 2–7 ppm), sample BBO6 in which Ni shows 58 to 91 ppm and sample BBO1D that displays 211 ppm in Zr (Fig. 8a). Fig. 8b shows the variation and statistical outliers of trace elements. The two sides of the box are not equivalent indicating a skewed or asymmetric distribution. The majority of elements have left-skewed, except Zr that its median value is closed to the box's lower values, consistent with right-skewed distribution. The concentrations of Zr (9-211 ppm), Ba (6-62 ppm), Ni (10-91 ppm) Zn (13-68 ppm) and V (9-77 ppm) have more variability relative with the other elements (Fig. 8b). The

Journal of Tertiary and Industrial Sciences *Vol. 6, No. 3, 2026*
ISSN 2709-3409 (Online)

median values of Zr (28 ppm), Ba (29 ppm), Ni (37 ppm) Zn (32 ppm) and V (23 ppm) are lower than those found in PAAS (Taylor and McLennan, 1985).

Element	SiO_2	Al_2O_3	$Fe_2O_{3(T)}$	MgO	CaO	Na_2O	TiO_2	P_2O_5	SO_3	Ba	Cd	Cr	Mn	Co	Cu	Ni	Pb	Sr	V	Y	Zn	Zr
SiO_2	1																					
Al_2O_3	0.41	1																				
$Fe_2O_{3(T)}$	-0.84	-0.80	1																			
MgO	-0.32	0.31	-0.11	1																		
CaO	-0.07	0.33	-0.30	0.84	1																	
Na_2O	-0.07	-0.26	0.05	0.08	0.46	1																
TiO_2	0.32	0.80	-0.70	0.64	0.71	-0.11	1															
P_2O_5	-0.05	0.66	-0.39	0.61	0.61	-0.14	0.76	1														
SO_3	0.63	-0.02	-0.37	-0.62	-0.38	0.31	-0.25	-0.57	1													
Ba	0.45	-0.19	-0.18	-0.60	-0.20	0.58	-0.41	-0.47	0.67	1												
Cd	-0.66	-0.54	0.75	-0.20	-0.11	0.27	-0.43	-0.17	-0.22	0.01	1											
Cr	0.59	0.69	-0.78	0.28	0.51	-0.09	0.76	0.69	-0.15	0.03	-0.48	1										
Mn	0.18	0.24	-0.34	0.58	0.83	0.38	0.64	0.31	-0.24	-0.01	-0.16	0.55	1									
Co	0.35	0.60	-0.62	0.58	0.80	0.14	0.89	0.56	-0.20	-0.14	-0.27	0.77	0.88	1								
Cu	-0.07	0.14	0.12	-0.35	-0.30	-0.18	-0.06	-0.29	0.09	0.08	0.38	-0.17	0	0.06	1							
Ni	0.23	0.58	-0.54	0.70	0.77	0.03	0.93	0.57	-0.21	-0.45	-0.33	0.57	0.75	0.88	-0.07	1						
Pb	0.09	-0.39	0.32	-0.90	-0.97	-0.37	-0.75	-0.64	0.38	0.34	0.21	-0.45	-0.76	-0.75	0.35	-0.82	1					
Sr	-0.09	-0.36	0.16	0.14	0.53	0.70	-0.03	0.10	-0.17	0.41	0.40	0.24	0.56	0.32	-0.21	0.06	-0.35	1				
V	0.52	0.91	-0.84	0.38	0.53	-0.17	0.93	0.72	-0.09	-0.18	-0.50	0.88	0.53	0.83	0.05	0.77	-0.54	-0.07	1			
Y	-0.30	-0.33	0.27	0.53	0.70	0.50	0.20	0.06	-0.40	-0.09	0.35	0.06	0.79	0.51	-0.05	0.43	-0.60	0.75	-0.03	1		
Zn	0.27	0.68	-0.61	0.71	0.75	-0.13	0.97	0.78	-0.37	-0.48	-0.40	0.78	0.68	0.88	-0.20	0.93	-0.78	0.08	0.87	0.31	1	
Zr	-0.48	-0.27	0.51	-0.13	0.01	0.18	-0.21	-0.15	-0.23	0.07	0.86	-0.25	0.12	0.06	0.70	-0.14	0.13	0.37	-0.22	0.42	-0.23	1

Figure 6. Pearson's correlation matrix for the Bidjouka IFs.

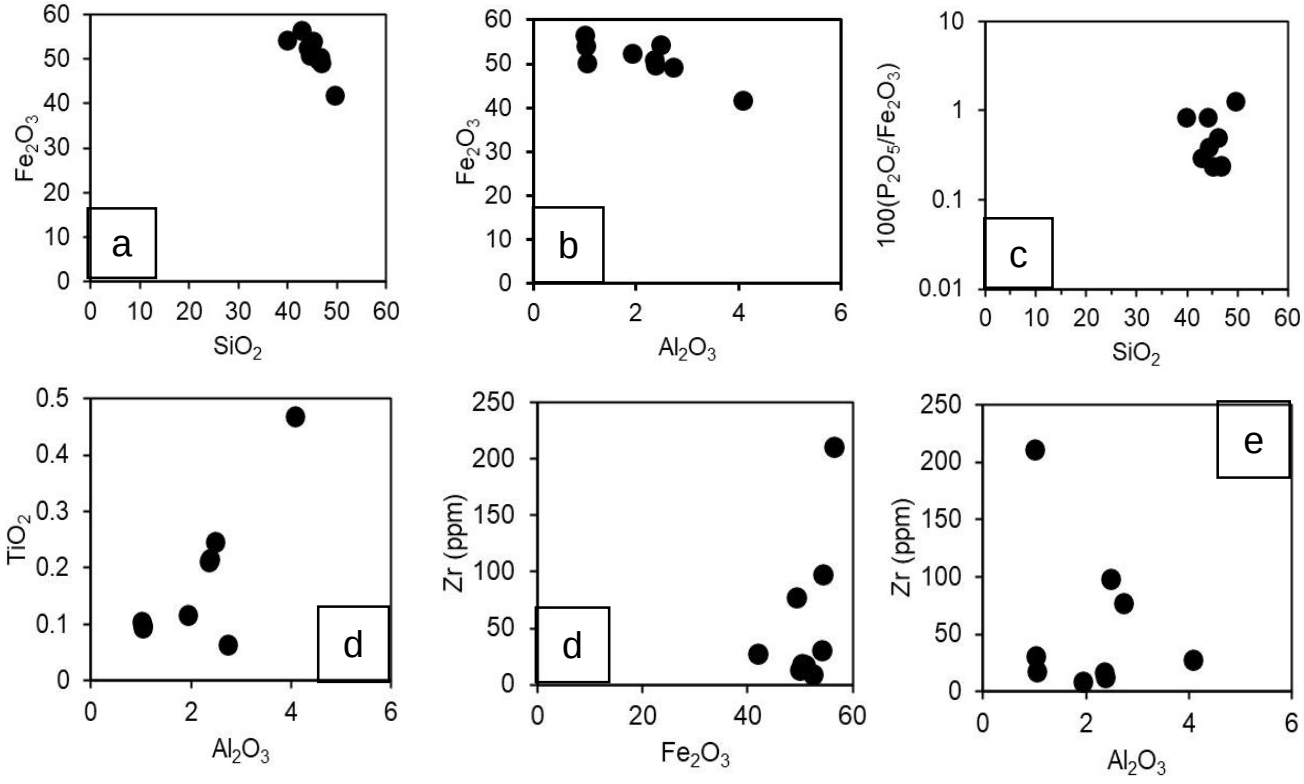

Journal of Tertiary and Industrial Sciences *Vol. 6, No. 3, 2026*
ISSN 2709-3409 (Online)

Figure 7. Variation diagrams for the Bidjouka BIFs. (a) biplot Fe_2O_3-SiO_2; (b) TiO_2-Al_2O_3 plot; (c) $100(P_2O_5/Fe_2O_3)$ vs. SiO_2 bivariate plot; (d) Zr vs Fe_2O_3, (e) Zr vs Al_2O_3.

4.2.3. Rare earth elements

The rare earth element (REE) distributions of the Bidjouka IF is reported in Table 2 The total rare earth element (ΣREE) contents range from 85.04 to 239.49 ppm (Table 2). The abundant of REE-Y ranges from 97.04 to 253.49 ppm. Normalization patterns (Fig. 8c) of REE using Post-Archaean Australian Shale (PAAS) by McLennan (1989) show relative rare earth elements fractionation (La_N/Yb_N = 0.79-4.23), relative light rare earth elements (LREEs) enrichment (La_N/Sm_N = 0.38–1.91) compared to heavy rare earth elements (HREEs, Tb_N/Yb_N = 7.29-9.56; La_N/Lu_N = 1.27–7.07), with a negative Eu anomaly (Eu/Eu* = 0.66-0.87) and a negative Ce anomaly (Ce/Ce* = 0.26-0.77; Fig. 8c).

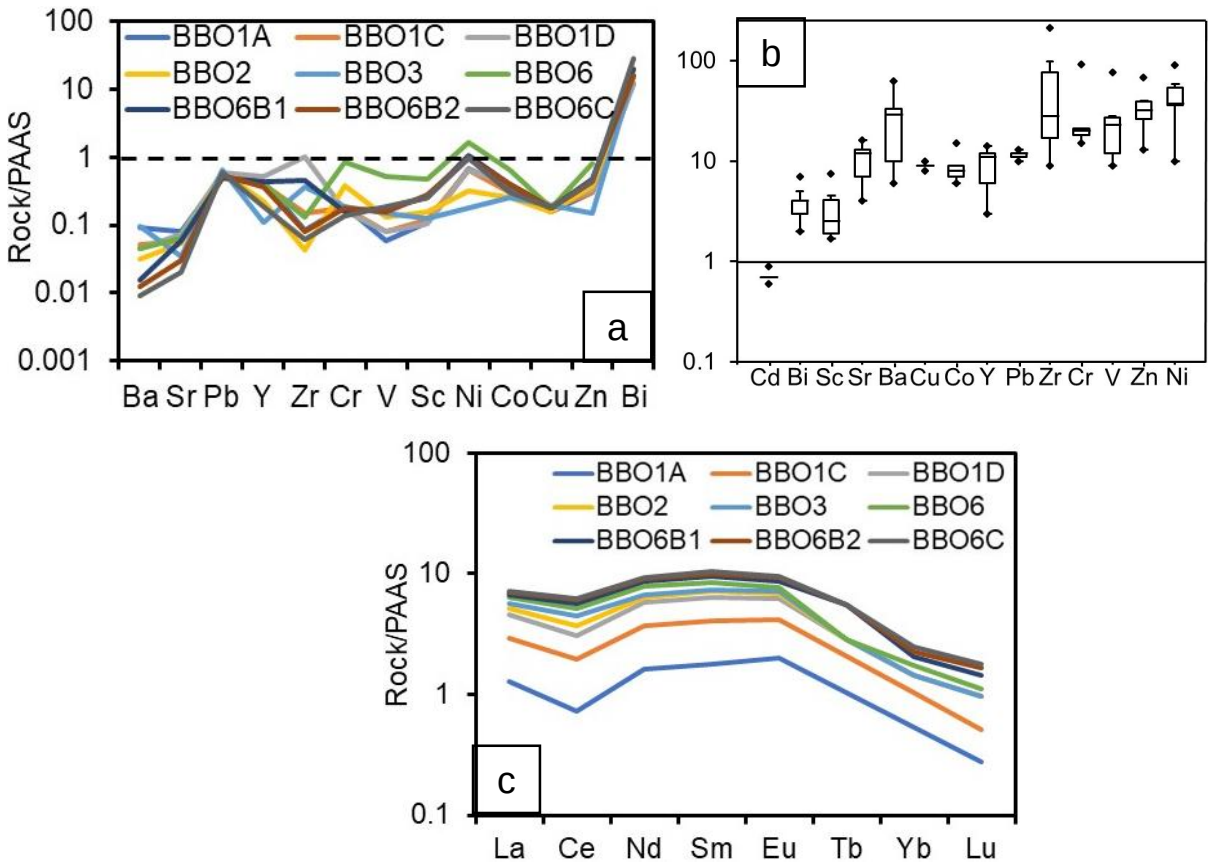

Figure 8. Range of trace element concentrations. (a) PAAS- normalized REEs spider diagram, (b) box plot showing the variation of trace elements and (c) PAAS- normalized REEs for the Bidjouka BIFs.

Journal of Tertiary and Industrial Sciences *Vol. 6, No. 3, 2026*
ISSN 2709-3409 (Online)

4.2.3. p-value calculation

A multivariate analysis is applied to investigate the p-value of the studied BIF. Since major elements are expressed in wt.% and trace element in ppm, we applied the centered log-ratio transformation (clr) by Aitchison (1986) to normalize the geochemical data, and the results of clr is presented in Table 3. Positive clr refers to clr $Fe_2O_{3(T)}$ and clr SiO_2 are consistently dominant. These elements are enriched relative to geometric mean of the sample. Negative clr such as clr Na_2O, clr SO_3, and clr Mn are strongly negative in all samples. Outliers such as BB01 has very high clr Zr (0.0895) and clr P_2O_5 (-3.584), and BBO6 shows high clr TiO_2, clr P_2O_5, clr Cr, clr Ni, and clr V suggesting more detrital/mafic input (Table 3). The principal component analysis (PCA) is further generated from the clr data and the results presented in Table 4. PCA displays three principal components (PC1, PC2, and PC3) cumulating at 83.10%. PC1 account for 42.30% of the total variance and is positively loaded with clr Al_2O_3, clr TiO_2, clr P_2O_5, clr Cr, clr V, clr Ni, and clr Zn, and negative score include clr SiO_2 and clr Fe_2O_3. PC2 involves 28.70 % of the total variance and shows positive loading with clr Zr, clr Y, and clr Ba, and negative with clr MgO, clr CaO, and clr SO_3. PC3 account for 12.10% and include high positive loading formed by clr Mn, clr Cu, clr Co, clr CaO, and clr MgO and high negative loading made up with clr Na_2O, clr Pb, clr Al_2O_3, and clr P_2O_5. A permutation test 9999 permutations was ran on clr-data to test if PC1, PC2, and PC3 explain more variance that random noise (Table 4). Elements with p-value < 0.05 are bold, others are not significant contributors. The broken-stick expected for PC1, PC2, and PC3 is 14.20, 10.80, and 8.90%, respectively. PC1 is significantly driven by clr SiO_2, clr Al_2O_3, clr $Fe2O_3$, clr TiO_2, clr P_2O_5, clr Cr, clr Co, clr Ni, clr V, and clr Zn, while PC2 is significantly driven by clr MgO, clr CaO, clr Na_2O, clr SO_3, clr Ba, clr Sr, clr Y, and clr Zr. PC3 is significantly driven by clr Na_2O, clr Co, clr Mn, and clr Cu. The permutation p-value is $p < 0.001$ for PC1 and PC2, and $p = 0.084$ for PC3.

Table 3. clr-transformed geochemical data of Bidjouka BIF

Sample	BBO1A	BBO1C	BBO1D	BBO2	BBO3	BBO6	BBO6B1	BBO6B2	BBO6C
clr SiO_2	0.482	0.388	0.283	0.323	0.513	0.613	0.235	0.405	0.458
clr Al_2O_3	-1.784	-1.799	-1.816	-1.236	-0.938	-0.585	-1.020	-1054	-1.043
clr $Fe_2O_{3(T)}$	0.557	0.569	0.563	0.498	0.565	0.448	0.541	0.543	0.536
clr MgO	-1.784	-2.273	-2.036	-1.882	-4.679	-1.501	-1334	-1.362	-1.892
clr CaO	-2.496	-3.156	-2.929	-3.268	-4.396	-2.251	-2.28	-2.621	-3.338
clr Na_2O	-4.784	-5.296	-5.296	-5.694	-5.091	-5.296	-5.099	-5.694	-5.694
clr TiO_2	-4.145	-4.119	-4.064	-4.001	-4.535	-2.549	-3.095	-3.236	-3.220
clr P_2O_5	-3.914	-3.846	-3.584	-2.648	-3.914	-2.441	-2.610	-3.296	-3.079
clr SO_3	-6.396	-7.153	-7.494	-8.21	-6.396	-7.153	-8.210	-7.488	-6.614

Journal of Tertiary and Industrial Sciences *Vol. 6, No. 3, 2026*
ISSN 2709-3409 (Online)

clr Ba	-0.598	-1.184	-1.308	-1.607	-0.581	-1.277	-2.060	-2.271	-2.543
clr Cd	-3.154	-3.154	-2.904	-3.154	-3.154	-3.288	-3.030	-3.288	-3.154
clr Cr	-1.255	-1.296	-1.394	-0.577	-1.255	-0.215	-1.540	-1.386	-1.609
clr Co	-2.326	-2.443	-2.201	-2.575	-2.575	-1.690	-2.201	-2.201	-2.415
clr Mn	-6.703	-6.703	-6.703	-7.088	-7.088	-6.415	-6.688	-6.688	-7.088
clr Cu	-2.326	-2.201	-2.099	-2.326	-2.099	-2.201	-2.201	-2.201	-2.201
clr Ni	-0.788	-0.808	-0.808	-1.498	-2.090	-0.225	0.667	-0.729	-0.729
clr Pb	-2.011	-1.924	-1.924	-1.924	-1.847	-2.090	-2.090	-1.999	-1.924
clr Sr	-1.640	-1.924	-1.697	-2.000	-2.432	-1.868	-1.942	-2.551	-2.944
clr V	-2.207	-1.924	-1.924	-1.435	-1.304	-0.396	-1.320	-1.435	-1.285
clr Y	-1.924	-2.000	-1.766	-2.565	-3.258	-1.868	-1.781	-1.956	-2.648
clr Zn	-1.162	-1.162	-1.091	-0.952	-1.847	-0.189	-0.654	-0.677	-0.726
clr Zr	-1.540	-1.003	0.895	-2.140	-0.362	-1.343	-0.127	-1.827	-2.061

Table 4 Principal component analysis and p-values representation of Bidjouka BIF

Sample	PC1	PC1 p-value	PC2	PC2 p-value	PC3	PC3 p-value
clr SiO_2	-0.324	**0.002**	0.128	0.301	0.098	0.456
clr Al_2O_3	0.285	**0.009**	0.042	0.684	-0.201	0.156
clr $Fe_2O_{3(T)}$	-0.301	**0.004**	-0.051	0.639	-0.124	0.398
clr MgO	-0.112	0.298	-0.341	**0.001**	0.215	0.134
clr CaO	-0.108	0.321	-0.325	**0.002**	0.238	0.102
clr Na_2O	0.031	0.742	-0.201	**0.048**	-0.312	**0.037**
clr TiO_2	0.298	**0.005**	0.088	0.421	0.052	0.678
clr P_2O_5	0.276	**0.012**	0.102	0.321	-0.168	0.243
clr SO_3	-0.045	0.621	-0.318	**0.003**	0.089	0.492
clr Ba	-0.089	0.381	0.285	**0.005**	-0.142	0.312
clr Cd	0.018	0.871	-0.034	0.763	-0.178	0.218
clr Cr	0.312	**0.003**	-0.054	0.612	0.041	0.741
clr Co	0.198	**0.039**	0.054	0.612	0.298	**0.041**
clr Mn	-0.021	0.832	-0.152	0.187	0.402	**0.011**
clr Cu	0.145	0.142	0.062	0.528	0.341	**0.028**
clr Ni	0.308	**0.004**	-0.038	0.703	0.035	0.782
clr Pb	0.052	0.0621	-0.089	0.441	-0.254	0.089
clr Sr	-0.062	0.568	-0.241	**0.029**	0.187	0.201
clr V	0.321	**0.002**	-0.021	0.821	-0.028	0.821
clr Y	-0.078	0.445	0.298	**0.003**	-0.065	0.612
clr Zn	0.287	**0.008**	0.011	0.912	-0.091	0.487
clr Zr	-0.102	0.312	0.341	**0.001**	0.087	0.501

Journal of Tertiary and Industrial Sciences *Vol. 6, No. 3, 2026*
ISSN 2709-3409 (Online)

Variance	42.30%		28.70%		12.10%	
Cumulative	42.30%		71.00%		83.10%	
Broken-stick expected	14.20%		10.80%		8.90%	
Permutation p-value		**p<0.001**		**p<0.001**		p = 0.084%

Bold: element with p-value < 0.05

5. Discussion

5.1. Iron occurrence

The BIFs of the Bidjouka area are regarded as chemical sedimentary rocks that were formed in the Precambrian (Klein, 2005). The sediments underwent diagenetic and metamorphic changes. Considering that the samples were taken from the surface, it is worth assuming their supergene alteration, during which some components can be leached (carbonates, silicates, sulfides), and oxides can be transformed (martitization of magnetite). Accordingly, the changes will also affect the chemical composition. The Bidjouka iron ore is part of greenstones belt of the Ntem Complex located in the Congo Craton (Nédélec et al., 1993). The BIFs of Bidjouka area are banded or laminated with alternating layers of iron-rich and silica-rich minerals. They are moderately to strongly magnetic suggesting the predominance of magnetite which is a strongly magnetic iron oxide mineral relative to hematite. As these BIFs indicate de presence of economic iron deposits, they can be a target for iron ore exploration. The mineralogy recorded consists of biotite, quartz, and magnetite/hematite and the characteristic of the recorded foliation (banding and schistosity underlined by a preferred orientation of stretched quartz and magnetite and/or hematite crystals; Fig. 4c) indicates that the studied rocks experienced S_1 foliation related to D_1 deformation.

5.2. Geochemical characteristics

The contents of SiO_2 (avg.: 44.99 wt.%) and Fe_2O_3 (avg.: 51.07 wt.%) in the Bidjouika BIFs indicate the purity of chemical precipitates. This suggest a classic taconite-grade BIF, not direct shipping ore (DSO). This supports the predominance of quartz and iron oxide (magnetite/hematite) in the studied BIFs. The presence of these two components suggests that the Bidjouka iron deposits can be classified as oxide facies BIF (James, 1992). This aligns with the works of Rosière et al. (2018) and James (1992) indicating that BIFs widely occur in greenstone belts and supracrustal sequences, with the occurrence of oxide, silicate, carbonate and sulfide facies. The geochemical characteristics of their formation suggest the processes of deep differentiation of the material in the formation of the IFs (Mel'nik 1982). The oxide facies of the studied BIFs is composed of quartz as the main gangue mineral, associated with iron oxides (magnetite/hematite). This result is common for the majority of the studied BIFs in Cameroon (Ndema et al., 2022b; Tamehe et al., 2019). High field strength elements (HFSE) like TiO_2

Journal of Tertiary and Industrial Sciences *Vol. 6, No. 3, 2026*
ISSN 2709-3409 (Online)

(<0.5 wt.%) and Y (3-14 ppm) suggest distal hydrothermal + water source. The calculated correlation matrix shows that the reported correlations are statistically significant (Fig. 6). The strong negative correlation between Fe_2O_3 and SiO_2 (r = -0.84) reflects the primary binary Fe-Si component of the BIF and indicates minimal detrital contamination. This binary mixing trend (Fig. 7a) is typical for chemical sedimentary in BIFs and suggests that major element variations are controlled mainly by the relative proportion of Fe-oxide and quartz bands rather than by aluminous detritus. Penalty element such as $P_2O_5 \leq 0.02\%$ wt.% are very low and good for direct reduced iron (DRI) pellets. The Al_2O_3 (1.01 to 4.08 wt.%; avg.: 2.11 wt.%) content recorded suggests clastic input from the continent into the ocean during the precipitation of BIF. In Addition, Al_2O_3 displays a positive correlation with TiO_2 (Fig. 7b), this could be inherited from the common association of Ti and Al in clay derived from weathering materials. This is consistent with the work of Adekoya et al. (2012). The Bidjouka BIFs display high Al_2O_3 (avg.: 2.11 wt.%) content relative to that of typical IFs which are generally lower than 1.5%. Thus, before interpreting the geochemical tracers in term of depositional processes, the potential impact form syn-depositional clastic contamination should be evaluated (Barrett, 1981; Hu et al., 2017). This is because minor clastic materials, when incorporated into IFs during depositional processes, are sufficient to obscure original marine signatures. The BIFs show positive correlations between Al_2O_3 and TiO_2 (r = 0.80), V (r = 0.91) and Cr (r = 0.69) and the covariation graph Zr-Al_2O_3 (Fig. 7f) suggesting a terrigenous contribution during the deposition. This is consistent with work of Hu et al. (2017). The correlation diagram of Zr-Fe_2O_3 (Fig. 7e) also corroborates with the incorporation of iron components from the continental source and indicates the inputs of Zr from the detrital Zr-rich minerals in the BIFs. This result aligns with the study of Aftabi et al. (2021). We used the following formula to determine the detrital input of the Bidjouka BIFs:

$$\% \text{ detritus} = 100 \times (X_{sample}/X_{MQS}), \quad (10)$$

where Xsample refers to Al_2O_3 in the analyzed BIF and $X_{MQS} = 17.3\%$ denotes the average Al_2O_3 in the muscovite–quartz schist. Applying this equation, the Bidjouka BIFs contain 5.54–23.58 wt.% (avg.: 12.20 wt.%) detrital inputs. This value of detrital contamination reflect deposition in a distal. Therefore, the low grade of Al_2O_3, TiO_2, and P_2O_5 contents, coupled with High SiO_2-Fe_2O_3, indicate The Bidjouka BIF is a Superior-type chemical sediment that reflects deposition in a distal, chemically-dominated basin with minimal terrigenous input, consistent with Superior-type BIF. The geochemistry is consistent with precipitation in a passive margin setting with seawater and moderate continent al input. The limited upper range suggests the absence of significant volcaniclastics and indicates that post-depositional aluminous alteration was not pervasive. In addition, the Bidjouka iron ore shows elevated rare earth element concentration with ΣREE ranging from 85.04 to 239.49 ppm (Table 2). The elevated REE of IFs is the consequence of terrigenous inputs to the chemical precipitate (Arora et al., 1995). This is also supported with the strong negative correlation observed between Al_2O_3 and Fe_2O_3 (r = 0.80), suggesting mixing between a Fe-rich chemical precipitate and Al-

Journal of Tertiary and Industrial Sciences *Vol. 6, No. 3, 2026*
ISSN 2709-3409 (Online)

rich detrital component. The trend (Fig. 7b) indicates minimal terrigenous contamination during deposition and is consistent with a Superior-type BIF protolith. Samples deviating toward higher Al_2O_3 may reflect aluminous hydrothermal alteration associated with shear zones.

Applying PCA results, PCA displays three mains component: PC1, PC2, and PC3. PC1 shows positive and negative loading. Positive loading score including Al_2O_3, TiO_2 P_2O_5, Cr, V, Ni, and Zn characterizing detrital/mafic input, while negative loading (SiO_2 and Fe_2O_3) represent pure chemical BIF end-member (Table 4). PC2 is mainly a hydrothermal component composed of positive score loading Zr, Y, and Ba representing hydrothermal clastic zircon input. However, MgO, CaO, and SO_3 show negative loading compatible with carbonate/sulfide depletion. PC3 is make by transition metal formed with high positive loading score (Mn, Cu, Co, CaO, MgO) reflecting minor carbonate + redox-sensitive metal variability. Negative loading scores found in this component (Na_2O, Pb, Al_2O_3, P_2O_5) suggest depletion of alkalis and some detrital elements. Permutation testing confirms that PC1 and PC2 are significant ($p < 0.001$) and together explain 71% of total variance. They capture real structure in the data or the main geochemical processes at the Bidjouka, not random noise. PC3 explains 12.10% of total variance and was not statistically significant ($p = 0.084$), it below the 95% significant threshold ($p < 0.05$ is significant at 95% confidence), and it captures residual Na_2O-Co-Mn-Cu, variability (Table 4).

The Bidjouka BIFs show variable ratios in Al/(Al + Fe + Mn), Fe/Ti and Fe/Al in the range of 0.01–0.07, 104.36–883.68 (avg.: 467.67) and 13.56–73.92 (avg.: 40.67), respectively; this is due to the contribution of hydrothermal deposits by terrigenous deep-sea and pelagic sediments. Pure chemical sediments show enrichment in Mn and Fe, and pure hydrothermal deposit contains little Al and high Al/Ti ratio (Barrett, 1981). Addition of Al–rich and Ti–rich detrital inputs to hydrothermal sediments reduces the Fe/Ti ratios and increases the proportion of Al (Barrett, 1981; Xu et al., 2014). Furthermore, the ternary diagram Fe-Al-Mn (Boström, 1973) illustrates that the Bidjouka BIFs plot in the field of hydrothermal (Fig. 9a), suggesting that Si and Fe derive from hydrothermal sources. Therefore, the iron mineralization was formed through the precipitation of iron and silica from a mixture of seawater and low-temperature hydrothermal fluids. This is consistent with the works of Ebotehouna et al. (2021a), Tamehe et al. (2018), and Ndema and Aroke (2020). Since the Bidjouka iron deposit exhibits low content in Al_2O_3 and elevated Al/Ti ratios (7.70–37.08), the geochemical evidence suggests predominantly chemogenic precipitation with minor detrital input. The average Al/Ti ratio (12.81) is similar with the mean ratio of Al/Ti (13.36) in Ilaro formation (Madukwe et al., 2016). Also, the K_2O/Al_2O_3 ratio < 0.02 (Table 2) indicates a little input of alkali feldspars.

The Bidjouka BIFs display variable Si/Al ratio (10.10–39.58; avg.: 23.29; Table 2) and in the SiO_2 vs. Al_2O_3 diagram all the samples fall in the field of hydrothermal origin (Fig. 9b). Therefore, the source of iron was derived from hydrothermal fluids released into the deep-ocean (Toth, 1980). Eu anomalies

Journal of Tertiary and Industrial Sciences *Vol. 6, No. 3, 2026*
ISSN 2709-3409 (Online)

can be estimated to assess the hydrothermal fluids temperature. Positive Eu anomalies reflect high temperature hydrothermal fluids (T > 250°C). Slightly to null anomaly indicates low-temperature hydrothermal fluids (T < 200°C; Basta et al., 2011).

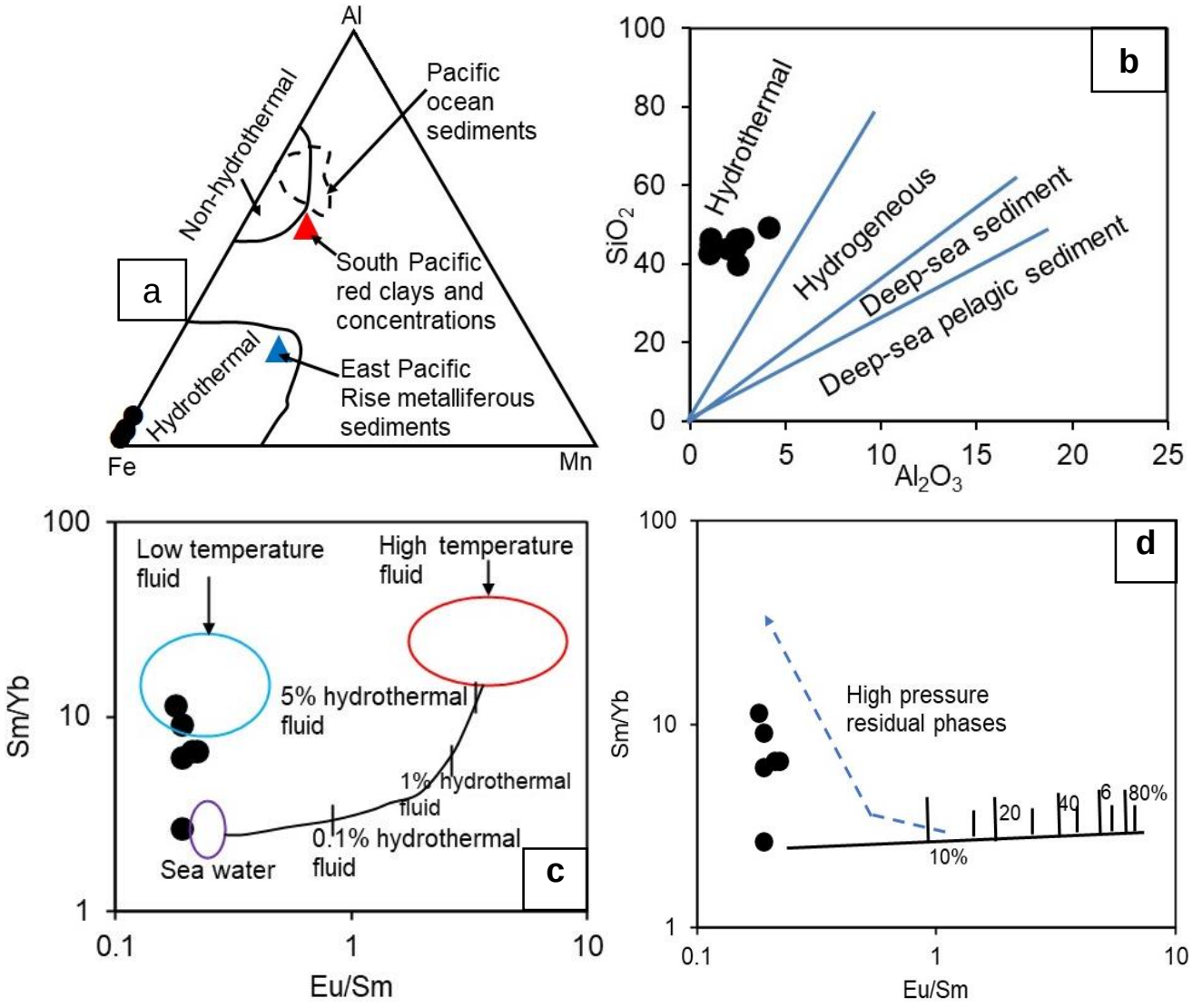

Figure 9. Discriminative diagrams of Bidjouka IFs. (a) Fe-Al-Mn ternary plot after Boström (1973); (b) SiO_2 vs. Al_2O_3 plot after Bonatti (1975); (c) Sm/Yb vs. Eu/Sm diagram modified after (Alexander et al., 2008); (d) plot of the composition of the studied rocks in the diagram Eu/Sm – Sm/Yb plot (Gourcerol et al., 2016).

The Bidjouka iron formations show weakly negative Eu anomaly (Eu/Eu* = 0.66-0.87; Table 2; Fig. 8c), this signal could be a signature inherited from low-T hydrothermal fluids (< 0.1%). The recorded weak negative Eu anomaly suggests depositional from seawater that was diluted by a detrital

Journal of Tertiary and Industrial Sciences *Vol. 6, No. 3, 2026*
ISSN 2709-3409 (Online)

component, with limited input from high-temperature hydrothermal fluids. These values are also consistent with a Superior-type BIF formed in a distal, relatively oxidized basin, rather than in a proximal volcanic setting. This result is also supported with the Sm/Yb vs. Eu/Sm plot (Alexander et al., 2008) in which most samples plot close to the field of hydrothermal fluid and only sample BBO6C plots close to the field of Sea water (Fig. 9c). The recent studies indicate that BIFs derived from mantle, seafloor, continent, or combination of the three sources and precipitated by hydrothermal solutions or seawater (Tamehe et al. 2021; Tchatchueng et al. 2021). The available literature shows that iron oxides in BIF and related iron ore reveal the abundance and ratios of a series of cations such as Al, As, Cu, Co, Cr, Ga, Mg, Mn, Mo, Ni, Sn, Ti, V, W, and Zn, compatible in iron oxides (Angerer et al. 2013; Duuring et al. 2020).

The Bidjouka BIFs display Sm/Yb and Eu/Sm ratios of 2.67-11.45 and 0.8-0.22, respectively (Table 2). The Sm/Yb vs. Eu/Sm plot (Gourcerol et al., 2016) is useful to estimate the depositional site relative to the hydrothermal source vent. Gourcerol et al. (2016) has demonstrated that samples closer to the high-temperature hydrothermal fluid end member indicate that the depositional site is near the hydrothermal source vent, while samples closer to the seawater end-member suggest a more distal depositional site. The Bidjouka BIF samples show value that reflect < 10% of a high-temperature hydrothermal fluid input. The graphical representation indicates that only sample BBO6C yields near the mixing line (Fig. 9d). This indicates that the depositional site of the Bidjouka BIF is more distal, similar to the result obtained in Gouap (Ndema and Mbonjoh, 2020) and Bateka (Ndema et al., 2022b). Furthermore, Sr, Rb, Ba and K are relatively immobile during metamorphism and therefore, help to assess the source characteristics of metasedimentary rocks. The studied BIFs have Ba and Sr contents of 6–62 ppm and 4–16 ppm, respectively with variable Ni contents (10–91 ppm; Table 2) consistent with mature sediment.

5.3. Comparison with global BIFs and with some know BIF deposits of the region

Compared to global BIFs of Lomagundi from Zimbabwe (Karhu and Holland, 1996; Martin et al., 2013) and Animikie (Lake Superior; Morey and Van Schmus, 1988; Johnston et al., 2006) as reported in Table 5, the BIF of Bidjouka is geochemically similar to the 2.1 Ga Lomagundi and 1.88 Ga Animikie BFIs. All three show Fe-Si correlations and moderate detrital input, consistent with Superior-Type deposition on passive margins. However, the weakly negative Eu anomaly in the studied BIF is lower than in most Animikie members and similar to Lomagundi BIFs, suggesting deposition in a distal basin with limited high-temperature hydrothermal input and an increasing oxidized water column in the mid-Paleoproterozoic.

The BIFs of the Bidjouka area were also compared with some known BIFs of the region, notably Elom (Ganno et al., 2015), Meyomessi (Ganno et al., 2018), Kpwa-Atog Boga (Tamehe et al., 2018), Edea

Journal of Tertiary and Industrial Sciences *Vol. 6, No. 3, 2026*
ISSN 2709-3409 (Online)

north (Mbang et al., 2017), Messondo (Ndema and Luku, 2020), and Nabeda (Ebotehouna et al., 2021a) areas. As far as the geological position is concerned, all these BIFs outcrop in the Congo Craton. The BIFs of Elom and Meyomessi areas are deposited in the Ntem complex in Cameroon, those of Nebeda area outcrop in the Ivindo Basement Complex in the Republic of Congo, while the BIFs of Bidjouka, Kpwa-Atog Boga, Edea north and Messondo area occur in the Paleoproterozoic Nyong Complex. The Paleoproterozoic Nyong Complex refers to the western border of the Ntem Complex. In term of petrography of rocks, the BIFs of Bidjouka area are made up of magnetite/hematite, quartzite (dominated magnetite mineral) similar to those of Elom, Meyomessi, Kpwa-Atog Boga, Edea north (including banded iron ores and massive iron ore facies), Messondo, and Nabeda (oxide and carbonate-oxide facies) areas. Like the majority of BIFs in the Ntem Complex in South Cameroon, the BIFs of the Bidjouka area are classified into oxide facies BIFs and differs from the silicate facies recorded in Messondo area (Ndema and Luku 2020), oxide facies, and carbonate-oxide facies reported in Nabeda area (Ebotehouna et al., 2021). Most BIF in Cameroon are classified into oxide facies, dominated either with hematite or magnetite. The study BIFs are enriched in SiO_2 and Fe_2O_3 similar to those reported in the region by Ganno et al. (2015; 2018), Tamehe et al. (2018), Mbang et al. (2017), Ndema and Luku (2020), and Ebotehouna et al. (2021; Fig. 10). BIFs from Nabeda areas displays in addition an enrichment in CaO (Fig. 10). There is no significant difference in major and trace element contents between the BIFs of Bidjouka area with the those from other regions within the northern border of the Congo Craton (Fig. 11).

Furthermore, the comparative normalized REE–Y profiles (Fig. 12) show that there is a significant degree of consistency and similarity between the Archean BIF from the Ntem and Ivindo Basement complex (Ganno et al., 201; 2018; Ebotehouna et al., 2021), the Paleoproterozoic BIFs from the Nyong Complex (Mbang et al., 2017; Tamehe et al., 2018; Ndema and Luku, 2020) as well as those of high- and low-temperature hydrothermal solutions. The Bidjouka BIFs are more enriched in REE (specially LREE) and Y compared with Elom, Meyomessi, and Seawater BIFs (Fig. 12).

Journal of Tertiary and Industrial Sciences *Vol. 6, No. 3, 2026*
ISSN 2709-3409 (Online)

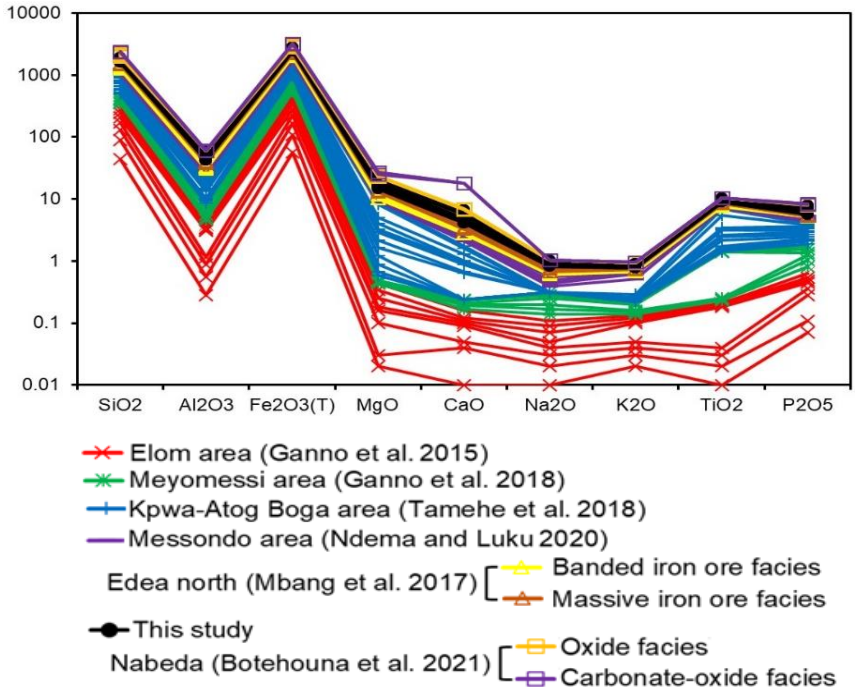

Figure 10. Spidergram comparing the BIF of the Bidjouka area with (i) the Archean BIF from the Ntem and Ivindo Basement complex (Ganno et al., 2015; 2018; Ebotehouna et al., 2021a) and (ii) the Paleoproterozoic BIFs from the Nyong Series (Mbang et al., 2017; Tamehe et al., 2018; Ndema and Luku, 2020) known in the region.

Journal of Tertiary and Industrial Sciences *Vol. 6, No. 3, 2026*
ISSN 2709-3409 (Online)

Table 5. Comparison with global BIFs.

Feature	Bidjouka BIF	Lomagundi BIF (Zimbabwe)[1, 2]	Animikie BIF (Lake Superior)[3, 4]
Age	Paleoproterozoic	2.1 Ga, peak Lomagundi Event	1.8 Ga, post-Lomagundi Event
Fe_2O_3/SiO_2	r = -0.84, strong binary	r = -0.80 to -0.90, very strong binary	r = -0.70 to -0.85, strong binary
Fe_2O_3/Al_2O_3	r = -0.80	r = -0.60 to -0.75, slightly more detrital	r = -0.75 to -0.85, clean
Detrital %	5.54-23.58%, avg.: 12.20%	8-20%, avg.: 14%	5-15%, avg.: 9%
Eu/Eu*	0.66-0.87, weak negative	0.70-1.10, weak negative to no anomaly	0.80-1.20, no anomaly to weak positive
Depositional setting	Distal, passive margin	Cratonic platform, shallow	Foreland basin passive margin
Ocean chemistry signal	Post-GOE, redox stratified	Peak of carbon burial, high O_2	Waning O_2 return to more anoxic deep water

[1)] Karhu and Holland (1996)
[2)] Martin et al. (2013)
[3)] Morey and Van Schmus (1988)
[4)] Johnston et al. (2006)

Journal of Tertiary and Industrial Sciences *Vol. 6, No. 3, 2026*
ISSN 2709-3409 (Online)

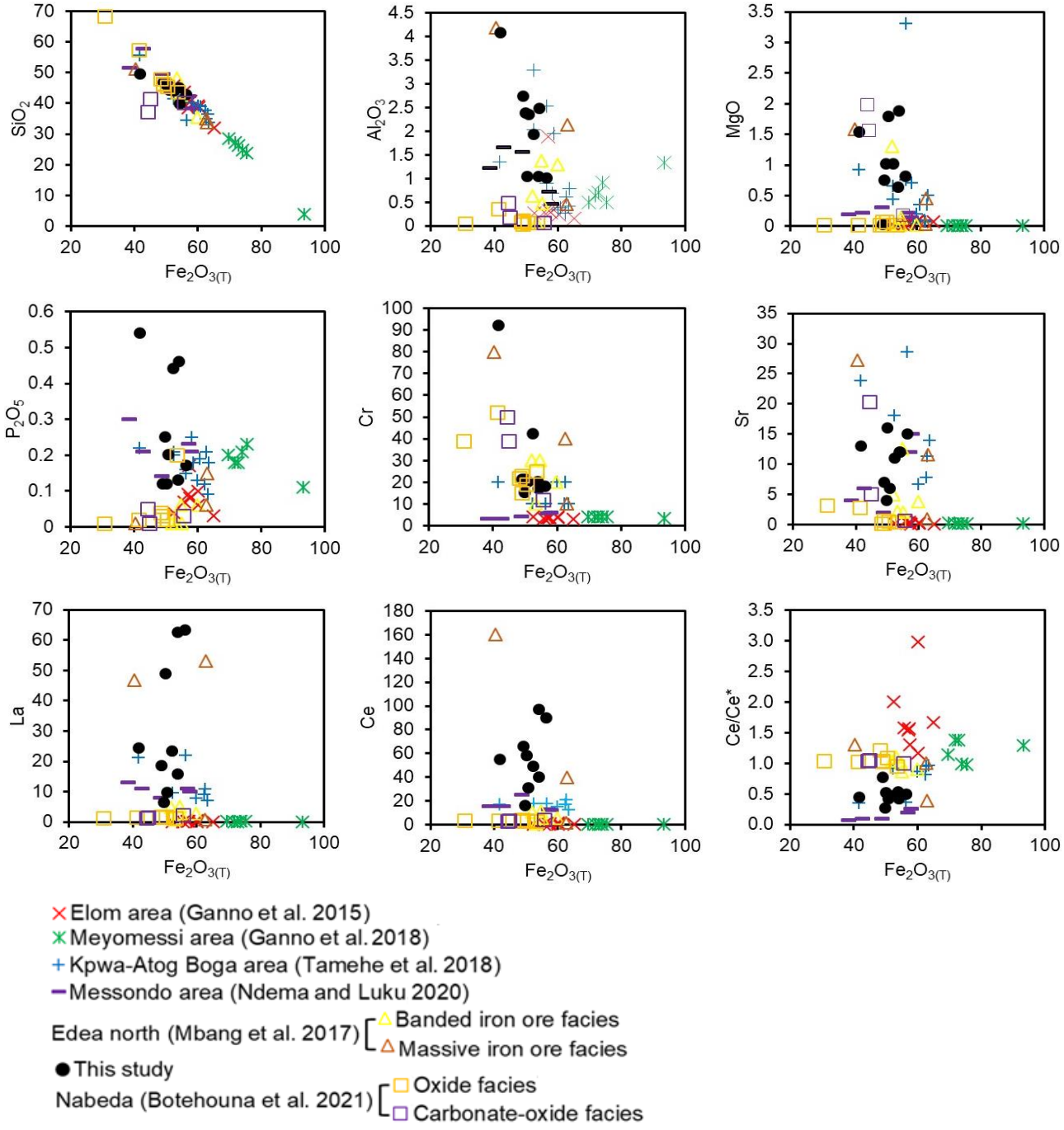

Figure 11. Variation diagrams of $Fe_2O3_{(T)}$ vs. some major and trace elements of the Bidjouka BIFs compared with Archean and Paleoproterozoic BIFs known of the region.

Journal of Tertiary and Industrial Sciences *Vol. 6, No. 3, 2026*
ISSN 2709-3409 (Online)

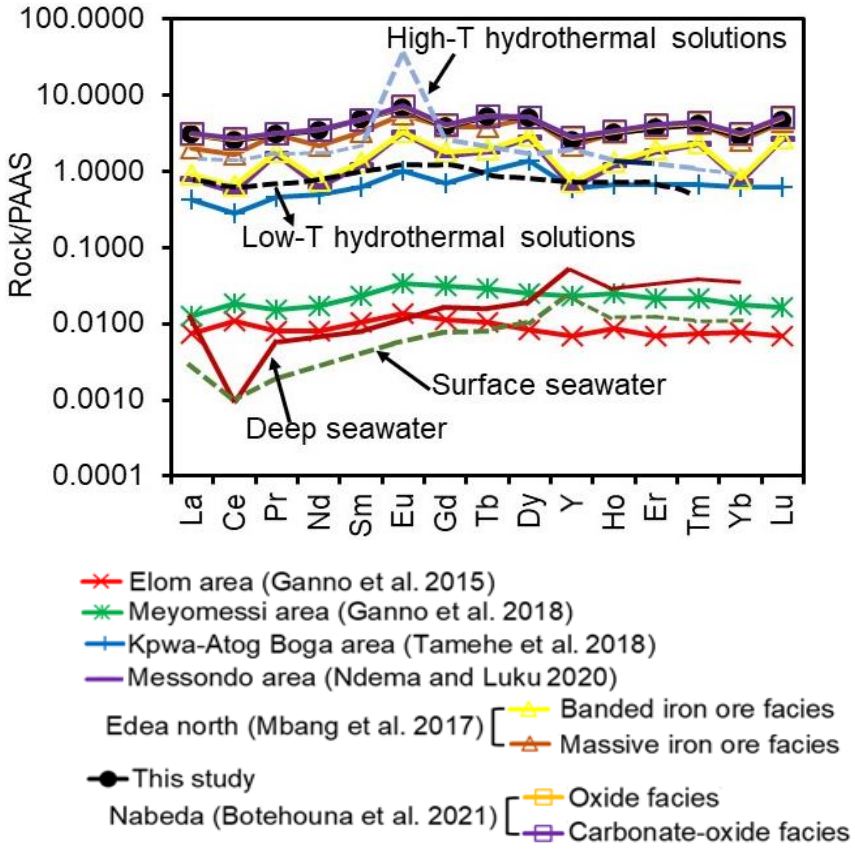

Figure 12. PAAS-normalized REE-Y profiles of the Bidjouka BIFs compared with the average contents of hydrothermal fluids (Bau M and Dulski, 1999), seawater (Bolhar et al., 2004), and some studied BIFs of the region.

5.4. Implications for Paleoproterozoic ocean chemistry and regional tectonic significance

Paleoproterozoic BIF are reported between 2.5 to 1.6 Ga, right after the Great Oxidation Event (GOE) that were occurred around 2.4 Ga. The weak negative Eu anomaly, moderate detrital contamination, and strong Fe-Si binary composition suggest deposition in a distal, chemically-dominated basin during the Paleoproterozoic. The absence of a positive Eu anomaly indicates limited input of high-temperature hydrothermal fluids and an oxidizing water column that destabilized Eu^{2+}. Combined with moderate Al_2O_3, this support a post-GOE ocean with an anoxic Fe^{2+}-rich deep layer overlain by oxygenated surface waters, consistent with deposition on a passive continental margin. The studied BIF was deposited in a distal Superior-type setting on a Paleoproterozoic passive continental margin.

Journal of Tertiary and Industrial Sciences *Vol. 6, No. 3, 2026*
ISSN 2709-3409 (Online)

This setting is analogous to 1.88 Ga Animikie Basin, which evolved from a back-arc to a foreland basin during the Penokean orogeny between 1.88-1.83 Ga (Schulz and Cannon, 2007; Muhling et al., 2026), and to Lomagundi-age BIFs deposited on stable cratonic platforms during the Paleoproterozoic oxygenation event. The Penokean orogeny involved collision of the Pembine-Wausau arc at around 1880 Ma followed by Marshfield terrane accretion, leading to northward thrusting and development of foreland basin in which the Animikie Group was deposited. The tectonic quiescence and limited hydrothermal input reflect a post-collisional, stable margin environment characteristic of mid-Paleoproterozoic BIF deposition. This contrasts with Algoma-type BIFs that form in arc/back-arc setting (greenstone belt) with high volcanic input and strong positive Eu anomalies.

5.4. Quality of ores

The studied ore is a banded magnetite/and or hematite BIF with chemically dominated precipitation. The depleted values in P_2O_5 (0.12–0.54 wt.%; avg.: 0.27 wt.%), TiO_2 (0.07-0.47 wt.%; avg.: 0.18 wt.%) and SO_3 (0.00–0.02 wt.%; avg. :0.01 wt.%) suggest low contribution of gangue or deleterious elements. The strong negative Fe_2O_3 vs. SiO_2/Al_2O_3 correlation indicates the gangue is mainly quartz and minor aluminosilicates. The acceptable concentrations of phosphorous and sulphur in commercial purpose is lower than 0.07% P and 0.1% S (Guider, 1981; Dobbins MS and Burnet, 1982). Majority of iron ore deposits occur in Precambrian domains and the classification of Fe ore is still in debate. We used the following classification that vary from one author to another to assessed the iron resources: (i) Belevtsev et al. (1991) classifies the exploited iron ores into (1) high grade iron ore with Fe > 65%, (2) medium grade iron ore (Fe: 52 - 65%), and (3) low grade iron ore (Fe < 52%). (ii) Li HM et al. (2014) recognized low grade iron ore (< 50% Fe) and high grade iron ore (> 50% Fe) iron ore. (iii) According to Spier et al. (2008), high-grade iron ore shows > 64% Fe. It is worthy to know that there is no general consensus for these classifications. The geochemical results show that Fe_2O_3 and SiO_2 are the main constituents of the Bidjouka BIFs, they represent 96 wt% of the chemical composition. The concentration of $Fe_2O_{3(T)}$ ranges from 41.86 to 56.49 wt% (avg.: 51.07%). Regarding these above terminologies, the Bidjouka BIFs can be classified as low-grade iron ores with the average $Fe_2O_{3(T)}$ content of 51.07 wt%.

The Bidjouka BIF has good benefication potential despite its sub-economic Fe grade. The ore consists of a banded Fe-oxides and quartz with moderate aluminosilicates contamination. Beneficiation through grinding followed by magnetic separation and reverse flotation is expected to produce a concentrate grading 62-66% Fe with SiO_2 <5%. The simple mineralogy, low sulfide content, and absence of deleterious elements suggest the ore is amenable to conventional processing similar to other Lake Superior-type deposits. Furthermore, field observations and petrographic studies revealed that the BIFs samples are massive, moderately to strongly magnetic, weathered, and composed of magnetite/hematite (which is the main ore mineral and displays coarse grained), quartz and biotite.

Journal of Tertiary and Industrial Sciences *Vol. 6, No. 3, 2026*
ISSN 2709-3409 (Online)

However, detailed mineralogy and pilot-scale test work is required to confirm liberation size and optimize reagent schemes.

The bulk geochemical composition of iron ore is used to assess iron ore resources (Angerer et al., 2012). This helps to identify carbonate- or silicate-rich zones in BIF and illustrates the evolution of hypogene hydrothermal alteration zones through time. Accordingly, in the discriminant diagram of SiO_2/Fe_2O_3 vs. $(MgO + CaO + MnO)/Fe_2O_3$ plot by Angerer et al. (2012), all the BIF samples occupy the field of low –grade carbonate and siliceous BIF (Fig. 9e), confirming the above results. The Bidjouka iron deposits exhibits averagely 2.11 wt.% Al_2O_3 and 0.27 wt.% P_2O_5 potentially suitable for commercial iron ore exploitation; meanwhile, the reserves of this deposit are not yet estimated. As far as economic implications are concerned, economic viability will be governed by deposit tonnage, grind size, access to cheap power and water, and logistic to port. Given growing regional steel demand in Central Africa, the deposit could support either concentrate export or an integrated pellet/DRI plant, subject to positive feasibility studies. Further metallurgical test work and infrastructure studies are required to de-risk the project.

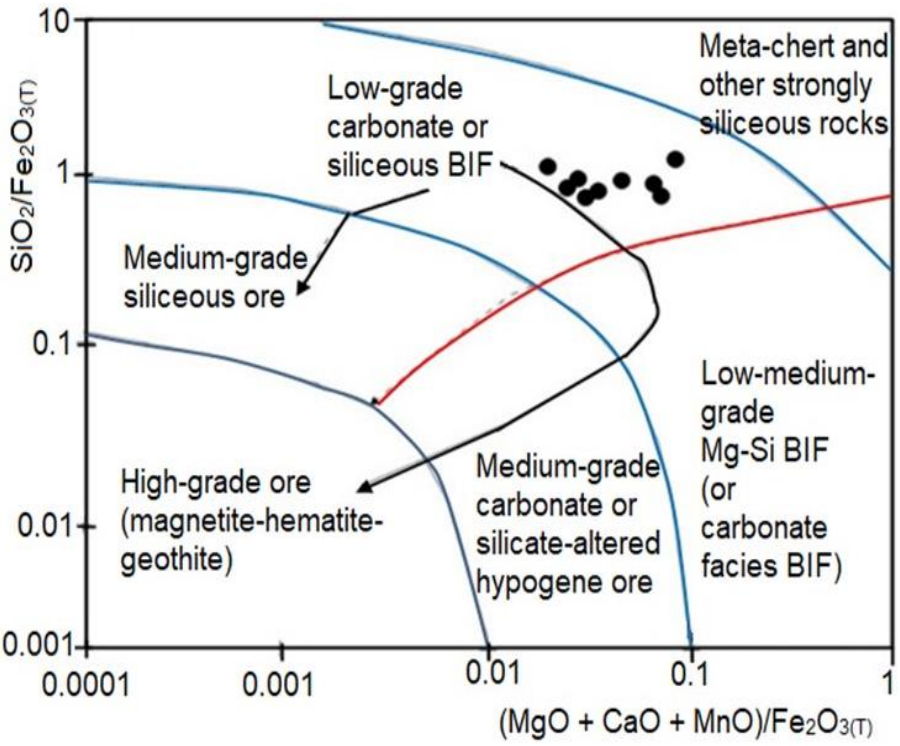

Fig. 13. Whole-rock $(MgO + CaO + MnO)/Fe_2O_{3(T)}$ vs. $SiO_2/Fe_2O_{3(T)}$ discrimination plot (Angerer et al., 2012).

Journal of Tertiary and Industrial Sciences *Vol. 6, No. 3, 2026*
ISSN 2709-3409 (Online)

5.5. Comparison with commercial iron ores and possible mining significance

Compared to commercial iron ores, the BIF of the Bidjouka area is mostly similar to Superior-type deposits of the Lake Superior region (Table 6). Unlike high-grade direct shipping ore (DSO) from, Brazil, the ore requires full beneficiation to reach marketable 62-66% Fe grades. The mineralogy is simpler than Harmersley ores with Fe-silicates and is compared to processed Mesabi taconites. The key competitive advantage would be proximity to growing Central Africa steel markets, while the main challenge is the energy and capital intensity required to upgrade low-grade primary BIF to pellet-grade concentrate.

The studied BIF has potential mining significance as a large-tonnage, low-grade iron resource. Although the ore requires beneficiation, its simple quartz-magnetite/hematite with minor biotite mineralogy and low impurity levels suggest it can be upgrade to marketable 62-66% Fe concentrate using conventional processing. If sufficient tonnage is confirmed, the deposit could serve growing regional steel demand in Central Africa and provide feedstock for pelletizing or direct reduction. The mining significance will ultimately depend on resource size, infrastructure development, and metallurgical test work. The deposit represents a promising iron or target analogous to the Lake Superior-type district.

Journal of Tertiary and Industrial Sciences *Vol. 6, No. 3, 2026*
ISSN 2709-3409 (Online)

Table 6. Comparison with commercial iron ores

Parameter	Bidjouka BIF	Lake Superior BIF (Mesabi, USA)[1]	Hamersley BIF (Pilbara, Australia)[2]	Direct shipping ore (DSO) Carajás, Brazil[3]	Magnetite DSO (Kiruma, Sweden)[4]
Ore type	Superior-type BIF	Superior-type BIF	Superior-type BIF	Hematite DSO	Magnetite DSO
Raw Fe grade	41.86-56.49 %	25-35%	30-35%	55-65%	35-45%
Gangue mineral	Quartz + minor clay/biotite	Quartz + clay	Quartz + clay	Goethite/kaolinite	Quart + apatite
Beneficiation needed	Yes, grind + magnetic separation + floatation	Yes	Yes	No, crushing + screening	Yes, grind + magnetic separation
Product grade	62-66% Fe potential	62-66% Fe pellets	62-66% Fe lump/fines	62-65% Fe lump/fines	65-70% Fe pellets
SiO_2 in product	3-5% target	3-5%	3-6%	3-6%	2-4%
Al_2O_3 in product	0.5-2% target	0.5-1.5%	1-2.5%	1-3%	0.5-1%
P	0.27%	<0.05	<0.08	0.05-0.10%	0.02-0.05%
S	Low - no sulfides indicated	Low	Low	Low	<0.01
Detrital input	5.5-23%, moderate	Low-moderate	Low	Variable	Very low
Eu anomaly	0.66-0.87, weak negative	Weakly negative	Weakly negative	Not analyzed - weathered	Slightly positive

[1)] Jirsa et al. (2008)
[2)] Trendall (2002)
[3)] Rosière and Rios (2004)
[4)] Parák (1975).

Journal of Tertiary and Industrial Sciences *Vol. 6, No. 3, 2026*
ISSN 2709-3409 (Online)

6. Conclusions

Results presented in this paper lead us to constrain several points for the Bidjouka banded iron formations:

1. The study of the Bidjouka IF provides the first geochemical and preliminary metallurgical characterization of BIF in the Nyong Complex. The Bidjouka iron deposit is a Paleoproterozoic Superior-type BIF formed in a passive margin setting and its study provides new constraints on Congo Craton evolution. Also, Bidjouka is a Cameroon's first documented large-tonne, low-grade BIF with potential for beneficiation, expanding the national iron ore resource model beyond high-grade DSO deposits.
2. At the regional level, this finding implies that (i) the geochemistry of the Bidjouka BIF confirms that the Nyong Complex records Paleoproterozoic 1.88-2.1 Ga passive margin sedimentation analogous to the Animikie Basin. This is a direct evidence linking the Southern Cameroon to global BIF-forming events during craton stabilization, suggesting that the other supracrustal units in the Nyong and Chailu Complexes may also host Superior-type BIF horizons that have been overlooked. Regionally, this reframes the Congo Craton margin as prospective for Animikie-style iron formation, not only Archean greenstone-hosted BIFs. (ii) The simple quartz-iron oxide ± biotite mineralogy of Bidjouka indicates that regional BIFs may be amenable to conventional beneficiation. Therefore, the Nyong, Ntem, and Chailu Complexes across Cameroon, Gabon, and Congo Republic should be prioritized for BIF exploration. Bidjouka thus serves as a type locality for a new iron ore district in Central Africa. (iii) Unlike the remote DSO deposits of Mbalam, Bidjouka is located in the South region with closer access to Kribi/Douala ports and the Central African, Chad, and Nigeria steel markets.
3. The BIFs have a chemogenic nature and formed in the Precambrian under different oceanic chemical conditions, the sediments underwent diagenetic and metamorphic changes. The source of iron was derived from hydrothermal fluids released into the deep-ocean, and the depositional site was more distal.
4. PC1 (Al_2O_3-TiO_2-P_2O_5-Cr-V-Ni-Zn) characterizes detrital/mafic input, while SiO_2-Fe_2O_3 represent pure chemical BIF end-member. PC2 is mainly a hydrothermal component in which Zr-Y-Ba represent hydrothermal clastic zircon input. and MgO-CaO-SO_3 reflects carbonate/sulfide depletion. PC3 is make by transition metals (Mn-Cu, Co-CaO-MgO) reflecting minor carbonate + redox-sensitive metal variability, and Na_2O-Pb-Al_2O_3-P_2O_5 suggest depletion of alkalis and some detrital elements. Statistically, PC1 and PC2 are significant while PC3 is not statistically significant, it captures residual Na_2O-Co-Mn-Cu, variability.

5. The Bidjouka iron ore deposit is a low-grade siliceous BIF, acceptable for commercial iron ores. The geological position, petrography of rocks, geochemistry, and origin of this iron ores deposit are fully compatible with that of Archean and Paleoproterozoic BIFs known of the region.
6. Central Africa hosts an underexplored Paleoproterozoic iron province. Future research work should focus on regional geochemical surveys, drilling, and pilot metallurgy to test the continuity and economic viability of Bidjouka and analogous BIFs, if proven, these deposits could form the basis of an integrated regional iron and steel industry.

7. Acknowledgments

The data presented in this paper represent part of the MSc thesis of the second author at the Department of Geology, University of Buea. The authors are indebted to anonymous reviewers and editor for their thoughtful and constructive comments.

8. References

Aitchison, J., 1986. The Statistical Analysis of Compositional Data. Chapman & Hall, New York, p. 416 pp.

Adekoya, A.J., Okonkwo, C.T., Adepoju, M.O., 2012. Geochemistry of Muro Banded Iron Formation, Central Nigeria. I J Geosci 3: 1074–1083.

Aftabi, A., Atapour, H., Mohseni, S., Babaki, A., 2021. Geochemical discrimination among different types of banded iron formations (BIFs): A comparative review. Ore Geol Rev. https://doi.org/10.1016/j.oregeorev.2021.104244.

Akagi, T., Masuda, A., 1998. A simple thermodynamic interpretation of Ce anomaly. Chem J 35(5): 301-314.

Akame, J.M., Debaille, V., Poujol. M., 2023. Combined bulk-rock Lu-Hf and Sm-Nd isotopic study of Archean granitoids and mafic rocks from Sangmelima terranes (Ntem Complex, south Cameroon): Geodynamic implications. Prec Res. https://doi.org/10.1016/j.precamres.2023.107072.

Akame, J.M, Oliveira, E.P., Poujol, M., Hublet, G., Debaille, V., 2020a. LA–ICP–MS zircon U/Pb dating, Lu/Hf, Sm/Nd geochronology and tectonic setting of the Mesoarchean mafic and felsic magmatic rocks in the Sangmelima granite-greenstone terrane, Ntem Complex (South Cameroon). Lithos. https://doi. org/10.1016/j.lithos.2020.105702

Akame, J.M., Owona, S., Hublet, G., Debaille, V., 2020b. Archean tectonics in the Sangmelima granite-greenstone terrains, Ntem Complex (NW Congo craton), southern Cameroon. J Afri Earth Sci. https://doi.org/10.1016/j.jafre arsci.2020.103872

Alexander, B.W., Bau, M., Andersson, P., Dulski, P., 2008. Continentally-derived solutes in shallow Archean seawater: rare earth element and Nd isotope evidence in iron formation from the 2.9 Ga Pongola Supergroup. South Africa. Geochim Cosmochim Acta 72: 378–394.

Angerer, T., Hagemann, S.G., Danyushevsky, L.V., 2013. High-grade iron ore at Windarling, Yilgarn Craton: a product of syn-orogenic deformation, hypogene hydrothermal alteration and supergene modification in an Archean BIF-basalt lithostratigraphy. Mineral Deposita 48(6): 697–728.

Arora, M., Govil, P.K., Charan, S.N., Uday Raj, B., Balaram, V., Manikyamba, C., Chatterjee, A.K., Naqvi, S.M., 1995. Geochemistry and origin of Archean banded iron–formation from the Bababudan Schist Belt, India. Econ Geol 2040–2057.

Barrett, T.J., 1981. Chemistry and mineralogy of Jurassic bedded chert overlying ophiolites in the North Appenines, Italy. Chem Geol 34:289–317.

Basta, F.F., Maurice, A.E., Fontboté, L., Favarger., P.Y., 2011. Petrography and geochemistry of the banded iron formation (BIF) of Wadi Karim and Um Anab. Eastern Desert. Egypt: Implications for the origin of Neoproterozoic BIF. Prec Res 187: 277-292.

Bau, M., Dulski, P., 1996. Distribution of yttrium and rare earth elements in the Penge and Kuruman Iron Formation, Transvaal Supergroup, South Africa. Prec Res 79:37–55.

Bau, M., Dulski, P., 1999) Comparing yttrium and rare earths in hydrothermal fluids from the Mid-Atlantic Ridge: implications for Y and REE behaviour during near–vent mixing and for the Y/Ho ratio of Proterozoic seawater. Chem Geol 55: 77–90.

Bekke, A., Holland, H.D., Wang, P-L., Rumble, III. D, Stein, H.J., Hannah, J.L., Coetzee, L.L., Beukes, N.J., 2004. Dating the rise of atmospheric oxygen. Nature 427: 117–120.

Bekker, A., Slack, J.F., Planavsky, N., Krapež, B., Hofmann, A., Konhauser, K.O., Rouxel, O.J. 2010. Iron formation: The sedimentary product of a complex interplay among mantle, tectonic, oceanic, and biospheric processes. Econ Geol 105: 467–508. https://doi:10.2113/gsecongeo.105.3.467.

Belevtsev, Y.N., Kravchenko, V.M., Kulik, D.A. et al. 1991. Precambrian banded iron formations of the European part of the USSR. Genesis of iron-ores. Naukova Dumka Press, Kiev, Ukrainia. (IGCP UNESCO Project. No. 247 (in Russian).

Beukes, N.J., Gutzmer, J., Mukhopadhyay, J., 2003. The geology and genesis of high-gade hematite iron ore deposits. Applied Earth Sci, 112: 18-25.

Bolhar, R., Kamber, B.S., Moorbath, S., Fedo, C.M., Whitehouse, M.J., 2004. Characterisation of early Archaean chemical sediments by trace element signatures. Earth Planet Sci Letters 222: 43–60.

Bonatti, E., 1975. Metallogenesis at oceanic spreading centers. Annu Rev Earth and Planet Sci 3: 401–431.

Boström, K., 1973. The origin and fate of ferromanganoan active ridge sediments. Stock. Contrib Geol 27:147–243.

Journal of Tertiary and Industrial Sciences *Vol. 6, No. 3, 2026*
ISSN 2709-3409 (Online)

Braga, F.C.S., Rosière, C.A., Pack, A., Hagemann, S.G., Santos, J.O.S., 2023. Oxygen isotopes of iron oxides as a diagnostic tool for iron formation-hosted high-grade magnetite-hematite deposits. Am J Sci. https://doi.org/10.2475/ 001c.88909.

Cloud, P., 1973. Paleoecological Significance of the Banded Iron-Formation. Econ Geol 68(7):1135–43. https://doi.org/10.2113/gsecongeo.68.7.1135

Cox, GM., Halverson, G.P., Minarik, W.G., Heron, D.P.L., Macdonald, F.A., Bellefroid, E.J., Strauss, J.V. 2013. Neoproterozoic iron formation: An evaluation of its temporal, environment al and tectonic significance. Chem Geol 362: 232–249.

Caen-Vachette, M., Vialette, Y., Bassot, J.P., Vidal. P., 1988. Apport de la géochronologie isotopique à la connaissance de la géologie gabonaise. Chronique Recherche Minière 491: 35-54.

Caxito, F.A., Santos. L.C.M.L., Ganade, C.E., Bendaoud, A., Fettous, E.H., Bouyo, H.M., 2020. Toward an integrated model of geological evolution for NE Brazil–NW Africa: the Borborema Province and its connections to the Trans-Saharan (Benino Nigerian and Tuareg shields) and Central African orogens. Special session. In Sial AN. and Ferreira VP (ed) A tribute to Edilton Santos, a leader in Precambrian Geology in Northeastern Brazil. Brazilian J Geol 50(2): 1–38. https://doi.org/10.1590/2317-48892 02020 190122.

Djoukouo, S.A.P., Ganno, S., Zhang, L.C., Tamehe, L.S., Wang, C.L., Peng, Z.D., Tong, XX., Nzenti, J.P., 2021. Geochemical and geochronological constraints on the origin of the Bibole banded iron formations, northwestern Congo Craton Cameroon: implications for their depositional age and tectonic environment. Geol Mag 158: 2245–2263. https://doi.org/10.1017/S0016.75682.10007.65.

Dobbins, M.S., Burnet, G., 1982. Production of an iron ore concentrate from the iron-rich fraction of power plant fly ash. Res Conservation 9: 231–242.

Duuring, P., Angerer, T., Hagemann, S.G., Banks, D.A., 2020. Iron deposits hosted by banded iron-formations in the Yilgarn Craton: Products of sequential iron enrichment by magmatic, marine and meteoric fluids. Ore Geol Rev 116: 103-251.

Douville, E., Bienvenu, P., Charlou, J.L., Donval, J.P., Fouquet, Y., Appriou, P., Gamo, T., 1999. Yttrium and rare earth elements in fluids from various deep–sea hydrothermal systems. Geochim Cosmochim Acta 63(5): 627–643.

Ebotehouna CG, Xie Y, Adomako-Ansah K, Gourcerol B, Qu Y (2021a) Depositional Environment and Genesis of the Nabeba Banded Iron Formation (BIF) in the Ivindo Basement Complex, Republic of the Congo: Perspective from Whole-Rock and Magnetite Geochemistry. Minerals. https://doi.org/10.3390/min11060579.

Ebotehouna, C.G., Xie, Y., Adomako-Ansah, K., Qu, Y., 2012b. Petrology, geochemistry, and zircon U–Pb-Lu–Hf isotopes of granitoids from the Ivindo Basement Complex of the Souanké Area, Republic of Congo: Insights into the evolution of Archean continental crust. Geol J 1–27. DOI: 10.1002/gj.4219.

Journal of Tertiary and Industrial Sciences *Vol. 6, No. 3, 2026*
ISSN 2709-3409 (Online)

Evina, A.Y.S., Odigui Ahanda, D.H., Ndjigui, P.D., Mvondo, O.J., 2023. Petrography, lithostratigraphy, and geochemistry of iron formations from Toko-Nlokeng area (northwestern Congo craton): Implications for origin, depositional tectonic setting, and potential iron ore resource deposit. Ore Energy Res Geol https://doi.org/10.1016/j.oreoa.2023.100020.

Feybesse, J.L., Johan, V., Maurizot, P., Abessolo, A., 1987. Evolution tectonom6tamorphique libérienne et éburnéenne de la partie NW du craton za'irois (SW Cameroun). In: Matheis G and Schandelmeier H (Ed), Current Research in African Earth Sciences, tome 2. Balkema, Rotterdam. p 9

Feybesse, J.L., Johan, V., Triboulet, C., Guerrot, C., Mayaga-Mikolo, F., Bouchot, V., Eko, N.J., 1998. The West Central African belt: a model of 2.5-2.0 Ga accretion and two-phase orogenic evolution. Prec Res 87: 161–216.

Ganno, S., Ngnotue, T., Kouankap, N.G.D., Nzenti, J.P., Notsa, F.M. 2015. Petrology and geochemistry of the banded iron-formations from Ntem complex greenstones belt, Elom area, Southern Cameroon: implications for the origin and depositional environment. Chemie der Erde 75: 375–387.

Ganno, S., Njiosseu, T.E.L., Kouankap, N.G.D., Djoukouo, S.A., Moudioh, C., Ngnotue, T., Nzenti, J.P., 2017. A mixed seawater and hydrothermal origin of superior-type banded iron formation (BIF)-hosted Kouambo iron deposit, Palaeoproterozoic Nyong series, Southwestern Cameroon: Constraints from petrography and geochemistry. Ore Geol Rev 80: 860–875.

Ganno, S., Tsozué, D., Kouankap, N.G.D., Tchouatcha, M.S., Ngnotue, T., Gamgne, T.R., Nzenti, J.P., 2018. Geochemical constraints on the origin of mineralized banded iron formation from the Meyomessi area, Archaean Ntem Complex (Congo Craton), southern Cameroon. Res Geol. http://dx.doi.org/10.1111/rge.12172.

Gourcerol, B., Thurston, P.C., Kontak, D.J., Côté Mantha, O., Biczok, J., 2016 Depositional setting of Algoma-type banded iron formation. Prec Res 281: 47–79. https://doi.org/10.1016/j.precamres.2016,04.019.

Guider, J.W., 1981. Iron ore beneficiation -key to modern steelmaking. Mineral Engineering 33:410–413.

Hagemann, S.G., Angerer, T., Duuring, P., Rosière, C.A., Silva, R.F., Lobato, L., Alde, D.H.G., 2016. BIF-hosted iron mineral system: a review. Ore Geol Rev 76: 317–359. https://doi.org/10.1016/j.oregeorev.2015.11.004.

Hinz, I.L., Nims, C., Theuer, S., Templeton, A.S., Johnson, J.E., 2021. Ferric Iron Triggers Greenalite Formation in Simulated Archean Seawater. Geol 49(8): 905–910. https://doi.org/10.1130/g48495.1

Hu, J., Wang, H., Wang, M., 2017. Geochemistry and origin of the Neoproterozoic Dahongliutan banded iron formation (BIF) in the Western Kunlun orogenic belt, Xinjiang (NW China). Ore Geol Rev 89: 836–857.

Huston, D.L., Logan, G.A., 2004. Barite BIFs and bugs: evidence for the evolution of the Earth's early hydrosphere. Earth Planet Sci Letters 220: 41–55.

Iglesias-Martínez, M., 2023. New occurrence of banded iron formations in the Minvoul Region, Ntem Complex (Northern Gabon). Iron Ore Conference, Perth, Australia, 18–20 September 2023.

James, H.L. 1992. Precambrian iron-formations: Nature, origin, and mineralogic evolution from sedimentation to metamorphism. In: Wolf KH and Chilingarian GV (ed) Diagenesis III, (Developments in Sedimentology), Elsevier Science, pp 543–589

James, H.L., Trendall, AF., 1982. Banded iron formation: Distribution in time and paleoenvironmental significance. In Holland HD and Schidlowski M (ed) Mineral Deposits and the Evolution of the Biosphere, Springer-Verlag, berlin Heidelberg, New York, pp 199-218

Jirsa, M., Miller, J., Morey, G.B., 2008. Geology of the Biwabik Iron Formation and Duluth Complex. Regulatory Toxicology and Pharmacology, 52 (1), S1-S9.

Johnson, J.E., Janet, R.M. Cosmidis, J., Rasmussen, B., Templeton, A.S., 2018. Low-Fe(III) Greenalite Was a Primary Mineral from Neoarchean Oceans. Geophys Res Letters, 45(7): 3182–92. https://doi.org/10.1002/2017gl076311.

Johnston, D.T., Poulton, S.W., Goldberg, T., Sergeev, V.N., Podkovyrow, V., Vorob'eva, N.G., Bekker, A., Knoll, A.H., 2006. Paleoceanographic constraints on Precambrian phosphorite accumulation, Baraga Group, Michigan, USA Sediment Geol, 226 (1-2), 9-21.

Kappler, A., Pasquero, C., Kurt, O.K., Newman, D.K. 2005. Deposition of Banded Iron Formations by Anoxygenic Phototrophic Fe(II)-Oxidizing Bacteria. Geol. https://doi.org/10.1130/g21658.1

Karhu, J.A., Holland, H.D., 1996. Carbon isotopes and the rise of atmospheric oxygen. Geol, 24, 867-870.

Klein, C., 2005. Some Precambrian banded-iron formation (BIFs) from around the world: their age, geologic setting, mineralogy, metamorphism, geochemistry and origin. Am Mineral 90: 1473–1499.

Koeksoy, E., Sundman, A., Byrne, J.M., Lohmayer, R., Planer-Friedrich, B., Halevy, I., Konhauser, K.O., Kappler, A., 2019. Formation of Green Rust and Elemental Sulfur in an Analogue for Oxygenated Ferro-Euxinic Transition Zones of Precambrian Oceans. Geol 47(3): 211–14. https://doi.org/10.1130/g45501.1

Kouayep, T.L.C., Ganno, S., Tamehe, L.S., Djoukouo, S.A.P., Fossi, D.H. Nzenti, J.P., 2024. Geochemistry and U-Pb zircon geochronology of the Nkout banded iron formations and associated metasiliciclastic rocks, NW Congo craton, southern Cameroon. I Geol Rev. DOI: 10.1080/00206814.2024.2326971

Kurzweil, F., Wille, M., Schoenberg, R., Taubald, H., Van Kranendonk, M.J., 2015. Continuously Increasing δ98 Mo Values in Neoarchean Black Shales and Iron Formations from the Hamersley Basin. Geochim Cosmochim Acta, 164: 523–42. https://doi.org/10.1016/j.gca.2015.05.009

Journal of Tertiary and Industrial Sciences *Vol. 6, No. 3, 2026*
ISSN 2709-3409 (Online)

Lerouge, C., Cocherie, A., Toteu, S.F., Penaye, J., Milési, J.P., Tchameni, R., Nsifa, E.N., Fanning, C.M., Deloule, E., 2006. Shrimps UPb zircon age evidence for Paleoproterozoic sedimentation and 2.05Ga syntectonic plutonism in the Nyong Group, South Western Cameroon: consequences for the Eburnean Transamazonian belt of NE Brazil and Central Africa. J Afri Earth Sci 44: 413-427.

Li, H.M., Zhang, Z.J., Li, L.X., Zhang, Z.C., Chen, J., Yao, T., 2014. Types and general characteristics of the BIF related iron deposits in China. Ore Geol Rev 57: 264–287.

Li, Y.L., Kurt, O.K., Zhai, M., 2017. The Formation of Magnetite in the Early Archean Oceans. Earth Planet Sci Letters 466: 103–14. https://doi.org/10.1016/j.epsl.2017.03.013.

Madukwe, H., Ogungbesan, G., Adeyinka, A., Ajisafe, Y., 2016. Provenance, Tectonic Setting, Source Area Weathering an Paleoenvironment of the Ilaro Formation, Dahomey Basi Nigeria. J Nigerian Soc Phys Sci 6(10): 96-119.

Martin, A.P., Condon, D.J., Prave, A.R., Lepland, A., 2013. A review of temporal constraints for the Paleoproterozoic. Earth and planet Sci Letters, 317-318, 295-304.

Maurizot, P., Abessolo, A., Feybesse, J.L., Johan, V., Lecomte, P., 1986. Etude et prospection minière du Sud-Ouest Cameroun. Synthèse des travaux de 1978 à 1985. Rapport BRGM., 85 CMR 066.

Mbang, B.B.M., Etame, J., Kouske, A.P., Bayiga, E.C., Ngon, N.G.F., Mbaï, S.J., Gérard, M., 2017. Ore Texture, Mineralogy and Whole Rock Geochemistry of the Iron Mineralization from Edea North Area, Nyong Complex, Southern Cameroon: Implication for Origin and Enrichment Process. I J Geosci 8: 659-677. https://doi.org/10.4236/ijg.2017.85036. 2017.

McLennan, SM., 1989. Rare earth elements in sedimentary rocks: influence of the provenance and sedimentary process. Rev Mineral Geochem 21: 169-200.

Mel'nik, YP., 1982. Precambrian banded iron-formations: physicochemical conditions of formation. In: Windley BF (ed) Developments in Precambrian Geology, 5th edn. Amsterdam - Oxford - New York, pp 1-307

Morey, G.B., Van Schmus, W.R., 1988. Correlation of Precambrian rocks of the Lake Superior region, United States. US. Geological Survey Professional Paper 1241-F, p. F1-F31.

Muhling, J.R., and Rasmussen, B., Zi, J.R., 2026. Timing of Penokean orogeny redefined: U-Pb ages from prekinematic monazite and xenotime in Lake Superior slates (Midwestern USA) indicate deformation spanned 1835-1760 Ma. Geol Soc Am, 1943-2682.

Mvodo, H., Ganno, S., Kouankap, N.G.D., Fossi, D.H., Nga Essomba, P.E., Nzepang, T.M., Nzenti, J.P., 2022. Petrogenesis, LA-ICP-MS zircon U-Pb geochronology and geodynamic implications of the Kribi metavolcanic rocks, Nyong Group, Congo craton. Acta Geochim. https://doi.org/10.1007/s11631-022-00533-2

Ndema, M.J.L., Aroke, E.A., 2020. Petrology and geochemical constraints on the origin of banded iron formation-hosted iron mineralization from the Paleoproterozoic Nyong Serie (Congo Craton,

South Cameroon), Pout Njouma Area (Edea North): Evidence for Iron Ore Deposits. International J Res Appl Sci 5(8): 55–72.

Ndema, M.J.L., Luku, O.I., 2020. Geology and geochemistry of Messondo banded iron formation-hosted iron ore from the northwestern Congo Craton, southern Cameroon: implication for iron ore deposits. Global Scientific J 8(2):4684-4699.

Ndema, M.J.L., Mbonjoh, T.M., 2020. Assessment of Banded Iron Formations around Gouap Area as Potential High-Grade Iron Ore (Nyong Serie, Congo Craton – South Cameroon). International Journal of Progressive Sciences and Technologies, 22(2): 87-110.

Ndema, M.J.L., Mukete, C.D., Djomo, M.C., Namange, P., 2024. Characterization of heavy minerals and stream sediment from Bidjouka area, Nyong Complex south Cameroon: implications for gold mineralization, Ore Energy Res Geol. https://doi.org/10.1016/j.oreoa.2024.100039

Ndema, M.J.L., Sigué, C., Nzenti, J.P., Suh, C.E., 2022a. Mineral chemistry (EMPA) of monazites in metamorphic rocks from Edea region: implications of the monazite chemistry on the metamorphic evolution of the Nyong Complex. Arab J Geosci. https://doi.org/10.1007/s12517-022-10924-7

Ndema, M.J.L., Namange, P., Ngoran, G., Bafon, G., Nchimenyi, S., Yongye, M., Moundignigni, A.B., 2022b. Petrogenesis of the Bateka Iron Prospect (Lower Dja Series, Proterozoic Cover of the Congo Craton - Cameroon). Frontiers. 2(3): 124-142.

Ndema, M.J.L., Ngnotue, T., Ngo Nlend, C.D., Nzenti, J.P., Suh, C.E., 2014. Origin and evolution of the formation of the Nyong serie in the Western Border of the Congo Craton. Journal of Geosciences and Geomatics, 2(2): 62-75.

Ndema, M.J.L., Sigué, C., Nzenti, J.P., Suh, C.E., 2019. Structural Characterization of Outcrop-Scale in Edea and Eseka Area: Evidence for a Complex Polyphase Deformation in the Paleoproterozoic Nyong Serie (Congo craton South Cameroon). J Appl Geol Geophys 7(5):01-09.

Ndema, M.J.L., Nzenti, J.P., Suh, C.E., Sigue, C., 2025. Age of the granulitic metamorphism of the Nyong complex in the west border of Congo Craton, South Cameroon. Discover Geoscience, 3: 108. https://doi.org/10.1007/s44288-025-00225-3

Ndime, E.N., Ganno, S., Nzenti, J.P., 2019. Geochemistry and Pb-Pb geochronology of the Neoarchean Nkout West metamorphosed banded iron formation, southern Cameroon. I J Earth Sci 108: 1551–1570.

Nédélec, A., Minyem, D., Barbey, P., 1993. High-P—High-T anatexis of Archaean tonalitic grey gneisses: The Eseka migmatites, Cameroon. Prec Res 62(3): 191–205.

Ngnotué, T., Ganno, S., Nzenti, J.P., Schulz, B., Tchaptchet, T.D., Suh, C.E., 2012. Geochemistry and geochronology of Peraluminous High-K granitic leucosomes of Yaoundé series (Cameroon): evidence for a unique Pan-African magmatism and melting event in North Equatorial Fold Belt. I J Geosci 3: 525–548.

Journal of Tertiary and Industrial Sciences *Vol. 6, No. 3, 2026*
ISSN 2709-3409 (Online)

Nzepang, T.M., Ganno, S., Okunloha, O.A., Njiosseu, T.N.E.L., Tamehe, S.L., Kamguia, W.B., Moto, M.A.S., Nzenti, J.P., 2021. Petrogenesis and tectonic setting of the Paleoproterozoic Kelle Bidjoka iron formations, Nyong Group greenstones belt, southwestern Cameroon: Constraints from petrology, geochemistry and LA-ICP-MS zircon U-Pb geochronology. I Geol Rev 63 (14): 1737–1757.

Ohmoto, H., Watanabe, Y., Yamaguchi, K.E., Naraoka, H., Haruna, M., Kakegawa, T., Hayashi, K.I., Kato, Y., 2006. Chemical and Biological Evolution of Early Earth: Constraints from Banded Iron Formations, Memoir Geol Soc Am 198: 291-331. https://doi.org/10.1130/2006.1198(17)

Owona, S., Ratschbacher, L., Gulzar, M.A., Nsangou, N.M., Mvondo, O.J., Ekodeck, G.E., 2020. New U-Pb zircon ages of Nyong Complex meta-plutonites: inferences on the Eburnean/TransAmazonian orogeny in SW Cameroon (Central Africa). Geol J 1–15. https://doi.org/10.1002/gj.4022

Owona, S., Ratschbacher, L., Nsangou, N.M., Gulzar, M.A., Mvondo, O.J., Ekodeck, G.E., 2021. How diverse is the source? Age, provenance, reworking, and overprint of Precambrian metasedimentary rocks of West Gondwana, Cameroon, from zircon U-Pb geochronology. Prec Res. https://doi.org/10.1016/j.precamres.2021.106220

Owona, S., Schulz, B., Minyem, D., Ratschbacher, L., Chako, T.B.C., Olinga, J.B., Mvondo, O.J., Ekodeck, G.E., 2022. Eburnean/Trans-Amazonian orogeny in the Nyong complex of southwestern Cameroon: meta-basite geochemistry and metamorphic petrology. J Afri Earth Sci. https://doi.org/10.1016/j.jafrearsci.2022.104515

Owona, S., Tichomirowa, M., Ratschbacher, L., Mvondo, O.J., Youmen, D., Pfänder, J.A., Affaton, P., 2012. New igneous (zircon Pb/Pb) and metamorphic (Rb/Sr) ages in the Neoproterozoic Yaoundé Group (Cameroon, Central Africa): Consequences for the orogenic evolution north of The Congo Craton. I J Earth Sci101(7): 1689–1703.

Parák, T., 1975. Kiruna iron ores are not magmatic. Econ Geol, 70 (7), 1242-1258.

Planavsky, N., Bekker, A., Rouxel, O.J., Kamber, B., Hofmann, A., Knudsen, A., Lyons, W.T., 2010. Rare Earth Element and yttrium compositions of Archaean and Paleoproterozoic Fe formations revisited: new perspectives on the significanceand mechanisms of deposition. Geochim Cosmochim Acta, 74: 6387–6405.

Planavsky, N., Reinhard, C.T., Wang, X., Thomson, D., Mcgoldrick, P., Rainbird, R.H. et al. 1014. Low Mid-Proterozoic atmospheric oxygen levels and the delayed rise of animals. Science. 346: 635–638.

Pouclet, A., Tcahameni, R., Mezger, K., Vidal, M., Nsifa, E.N., Shang, C., Penaye, J., 2007. Archaean crustal accretion at the Northern border of Congo Craton (South Cameroon): The charnockite-TTG ling. Bull Soc Géol France. 178:331-342.

Journal of Tertiary and Industrial Sciences *Vol. 6, No. 3, 2026*
ISSN 2709-3409 (Online)

Rosière, C.A., Heimann, A., Oyhantçabal, P., Santos, J.O.S., 2018. The iron formations of the South American Platform. In: Siegesmund S, Basei MAS, Oyhantçabal, P, Oriolo S (ed) Geology of Southwest Gondwana. Springer International Publishing, Cham, pp 493–526

Rosière, C.A., and Rios., F.J. 2004. The origin of Hematite ore bodies in the Quadrilátero Ferrífero, Minas Gerais, Brazil. Brazilian J. Geol, 34 (3), 125-144.

Schulz, K.J., and Cannon, W.F., 2007. The Penokean orogeny in the Lake Superior region. Prec Res, 157 (1-4), 4-25. DOI: 10.1016j.precamres.2007.02.022.

Spier, C.A., de Oliveira, S.M.B, Sial, A.N., Rosière, C.A., Ardisson, J.D., 2008. Mineralogy and trace-element geochemistry of the high-grade iron ores of the Aguas Claras mine and comparison with the Capão Xavier and Tamanduá iron ore deposits, Quadrilátero Ferrífero, Brazil. Miner Deposita, 43: 229–254.

Suh, C.E., Cabral, A, Shemang, E., Mbinkar, L., Mboudou, G., 2008. Two contrasting iron deposits in the Precambrian mineral belt of Cameroon, West Africa. Expl Mining Geol 17: 197–207.

Sun, L., Lechte, M., Shi, X., Zhou, X.., Zhou, L., Fang, H., Xie, B., Wu, M., Tang, D., 2022. Hexagonal Magnetite in Algoma-Type Banded Iron Formations of the Ca. 2.52 Ga Baizhiyan Formation, North China: Evidence for a Green Rust Precursor. Am Mineral 107(5): 970–84. https://doi.org/10.2138/am-2022-7981

Tamehe, L.S., Li, H., Ganno, S., Chen, Z., Lemdjou, Y.B., Elatikpo, S.M., 2024. Insight into the Origin of Iron Ore based on Elemental Contents of Magnetite and Whole-Rock Geochemistry: a Case of the Bipindi Banded Iron Formations, Nyong Complex, SW Cameroon. J Earth Sci. https://doi.org/10.1007/s12583-022-1622-4

Tamehe, L.S., Nzepang, T.M., Wei, C.T., Ganno, S., Ngnotue, T., Kouankap, N.G.D., Simon, S.J., Zhang, J.J., Nzenti, J.P., 2018. Geology and geochemical constrains on the origin and depositional setting of the Kpwa–Atog Boga banded iron formations (BIFs), northwestern Congo craton, southern Cameroon. Ore Geol Rev 95:620–638.

Tamehe, L.S., Wei, C.T., Ganno, S., Rosière, C.A., Nzenti, J.P., Ebotehoun, C.G., Lu, G., 2021. Depositional age and tectonic environment of the Gouap banded iron formations from the Nyong group, SW Cameroon: Insights from isotopic, geochemical and geochronological studies of drillcore samples. Geosci Frontiers 12:549–572.

Tamehe, L.S., Wei, C.T., Ganno, S., Simon, S.J., Kouankap, N.G.D., Nzenti, J.P., Lemdjou, Y.B., Lin, N.H., 2019. Geology of the Gouap iron deposit, Congo craton, southern Cameroon: implications for iron ore exploration. Ore Geol Rev 107: 1097–1128.

Tang, H., Chen, Y., 2013. Global glaciations and atmospheric change at ca. 2.3 Ga. Geoscience Frontiers. 4(5): 583-596. https://doi.org/10.1016/j.gsf.2013.02.003

Tarney, J., 1977. Petrology, Mineralogy and Geochemistry of the Farkland Plateau Basement Rocks. Site 330, Deep Sea Drilling Project, Initial Report. 36: 893-921.

Taylor, S.R., McLennan, S.M., 1985. The Continental Crust: Its Composition and Evolution. Blackwell, Oxford.

Tchameni, R., Mezger, K., Nsifa, N.E., Pouclet, A., 2001. Crustal origin of Early Proterozoic syenites in the Congo Craton (Ntem Complex), South Cameroon. Lithos. 5723–42.

Tchameni, R., Lerouge, C., Penaye, J., Cocherie, A., Milesi, J.P., Toteu, S.F, Nsifa, N.E., 2010. Mineralogical constraint for metamorphic conditions in a shear zone affecting the Archean Ngoulemakong tonalite, Congo craton (Southern Cameroon) and retentivity of U-Pb SHRIMP zircon dates. J Afri Earth Sci 58: 67–80.

Tchameni, R., Pouclet, A., K., Nsifa, N.E., Vicat, J.P., 2004. Monozircon and Sm-Nd whole rock ages from the Ebolowa greenstone belts: Evidence for the terranes older than 2.9 Ga in the Ntem Complex (Congo craton, South Cameroon). J Cameroon Acad Sci 4: 213–224.

Tchatchueng, R., Ngnotué, T., Njiosseu, T.E.L., Ganno, S., Wabo, H., Nzenti, J.P., 2021. Contrasting depositional environment of iron formation at Endengue Area, NW Congo Craton, Southern Cameroon: new insights from trace and rare earth elements geochemistry. I J Geosci 12(3): 280–306. https://doi.org/10.4236/ijg.2021.123016

Thiéblemont, D., Callec, Y., Fernandez-Alonso, M., Chène, F., 2018. A geological and isotopic framework of Precambrian Terrains in Western Central Africa: an introduction. In: Siegesmund S, Basei MAS, Oyhantçabal P, Oriolo S (ed) Geology of Southwest Gondwana. Springer International Publishing, Cham, 107–132. https://doi.org/10.1007/978-3-319-68920-3_5.

Toteu, S.F., De Wit, M., Penaye, J. et al. 2022. Geochronology and correlations in the Central African Fold Belt along the northern edge of the Congo Craton: new insights from U-Pb dating of zircons from Cameroon, Central African Republic, and south-western Chad. Gondwana Res 107: 296–324.

Toteu, S.F., Van Schmus, W.R., Penaye, J., Nyobé, J.B., 1994. U-Pb and Sm-Nd evidence for Eburnean and Pan-African highgrade metamorphism in cratonic rocks of southern Cameroon. Prec Res 67: 321- 347.

Toth, RJ., 1980. Deposition of submarine crusts rich in manganese and iron. Geol Soc Am Bull 91: 44–54.

Trendall, A.F., 2002. The geology of the Hamersley Province. Geological Survey of Western Australia, Bulletin 138, 513 p.

Van Schmus, W.R., Toteu, S.F., 1992. Were the Congo craton and the Sao Francisco craton joined during the fusion of Gondwanaland? Eos Trans AGU, 73(14), Spring Meeting Suppl., p. 365.

Xu, D.R., Wang, Z.L., Chen, H.Y., Hollings, P., Jansen, N.H., Zhang, Z.C., Wu, C.J., 2014. Petrography and geochemistry of the Shilu Fe-Co-Cu ore district, South China: Implications for the origin of a Neoproterozoic BIF system. Ore Geol Rev 57: 322–350.